

## Response to the editor's comments on manuscript gmd-2015-219 "An 11-year Global Gridded Aerosol Optical Thickness Reanalysis for Climate and Applied Sciences"

Dear Editor Olivier Boucher,

Thank you very much for reviewing this manuscript in detail and making a positive editorial decision on it. We appreciate your work. Here are our responses (in normal font) to your comments (*in italic*):

*1. "Applied sciences" in the title and in the text. I know this was a suggestion from one of the reviewer, but "applied sciences" sounds too broad. Maybe change to "atmospheric and climate sciences".*

Response: The title is now changed from "An 11-year Global Gridded Aerosol Optical Thickness Reanalysis for Climate and Applied Sciences" to "An 11-year Global Gridded Aerosol Optical Thickness Reanalysis (v1.0) for Atmospheric and Climate Sciences".

*2. It is now compulsory in GMD to number model versions in the title. Here I can only encourage you to number the version of your aerosol reanalysis, eg v1.0.*

Response: version number is now added in the title as shown in the response to the first comment.

*3. In the abstract, "applied applications" is redundant. Please amend.*

Response: "climate and applied applications" is replaced with "atmospheric and climate applications" in the abstract.

*4. Equation 1: Kz appears twice, I think this is a mistake. Please define the vertical coordinate sigma beyond saying it goes from 1 to 0. I don't think x and y are longitude and latitude, or you're missing some corrective factors to account for the sphericity of the Earth and the fact that a unit longitude is not the same at every latitude.*

Response: Thank you for capturing this mistake in the equation. Kz outside the bracket is removed. The description of the coordinates was "x and y are the horizontal coordinates (longitude and latitude),  $\sigma$  is the terrain-following vertical coordinate that ranges from 1 at the surface to 0 at the model top." Now it reads "x and y are the horizontal coordinates (in meter along longitude and latitude directions),  $\sigma$  is the terrain-following vertical coordinate ( $\sigma = p/p_s$ , where  $p$  is the present pressure and  $p_s$  surface pressure) that ranges from 1 at the surface to 0 at the model top."

*5. I think Hanel is Hänel (with a umlaut) throughout the manuscript.*

Response: "Hanel" is now replaced with "Hänel" throughout the manuscript.

6. Equation 5: it should be noted that Gamma is a function of sigma. Also the integral should be from 0 to 1, or strictly speaking tau is a negative number...

Response: As shown in line 221,  $\Gamma = d\sigma/dz$  ( $m^{-1}$ ). Because  $\sigma = p/p_s$ ,  $\Gamma$  has negative values. So tau in Equation 5 is a positive number, integrated over  $\sigma$  from 1 (surface) to 0 (top of atmosphere). Sorry for the confusion resulted possibly from the unclear definition of  $\sigma$ . Now with an explicit definition of  $\sigma$  as shown in our response to comment #4, equation 5 should make sense. As a result no change is made on equation 5.

7. Equation 6: Gamma (capital gamma) is already used, maybe gamma (small gamma) is more indicated for this exponent.

Response: Capital Gamma is replaced with small gamma ( $\gamma$ ) in equation 6 as suggested.

8. I prefer "550 nm" to "550nm" throughout the manuscript.

Response: "550nm" is replaced with "550 nm" throughout the manuscript and the SUPPLEMENTAL MATERIAL.

9. Equation 10: "scavenging" rather than "scavening"

Response: This typo is corrected.

10. Equation 12: can you say for which size range this corresponds to?

Response: yes. Added "for particles with diameters from 1.6 to 16  $\mu m$ " behind "where  $U_{10}$  is the wind speed at 10 meters above the sea surface in  $m s^{-1}$ ,  $a_s = 1.37 \times 10^{-13}$  and  $b_s = 3.41$ " and under equation 12.

11. Please change "6-hrly" to "6-hourly", no need for an abbreviation.

Response: all "6-hrly" are replaced with "6-hourly" throughout the manuscript.

12. Line 455: change AOD to AOT for consistency with the rest of the manuscript.

Response: All "AOD" are replaced with "AOT" throughout the text.

13. Line 464: change "grids" to "grid locations". Use italics for m and n in text.

Response: changes are made as suggested.

14. Line 477 and elsewhere: remove comma before year of reference.

Response: changes are made as suggested throughout the text.

15. *Line 237: change "optical depth" to "optical thickness" for consistency*

Response: "optical depth" is replaced with "optical thickness" throughout the manuscript.

1 **An 11-year Global Gridded Aerosol Optical Thickness Reanalysis (v1.0)**  
2 **for Atmospheric and Climate ~~and Applied~~ Sciences**  
3

4 Peng Lynch<sup>1</sup>, Jeffrey S. Reid<sup>2</sup>, Douglas L. Westphal<sup>2</sup>, Jianglong Zhang<sup>3</sup>, Timothy F. Hogan<sup>2</sup>, Edward J.  
5 Hyer<sup>2</sup>, Cynthia A. Curtis<sup>2</sup>, Dean A. Hegg<sup>4</sup>, Yingxi Shi<sup>3</sup>, James R. Campbell<sup>2</sup>, Juli I. Rubin<sup>5</sup>, Walter R.  
6 Sessions<sup>1,6</sup>, F. Joseph Turk<sup>7</sup>, and Annette L. Walker<sup>2</sup>

7

- 8 1. Computer Sciences Corporation Inc., Monterey, CA, USA  
9 2. Marine Meteorology Division, Naval Research Laboratory, Monterey, CA, USA  
10 3. Dept. of Atmospheric Science, University of North Dakota, Grand Forks, ND, USA  
11 4. Dept. of Atmospheric Science, University of Washington, Seattle, WA, USA  
12 5. National Research Council Postdoctoral Research Associate, Monterey, CA, USA  
13 6. Dept. of Atmospheric and Oceanic Sciences, University of Wisconsin-Madison, WI, USA  
14 7. Jet Propulsion Laboratory, Pasadena, CA, USA

15

16 Correspondence to: Peng Lynch, CSC Inc., Mail: Marine Meteorology Division, Naval Research  
17 Laboratory, 7 Grace Hopper Ave, Stop 2, Monterey, CA 93943. Email: peng.lynch.ctr@nrlmry.navy.mil

18

19 **Abstract**

20 While standalone satellite and model aerosol products see wide utilization, there is a significant  
21 need in numerous atmospheric and climate ~~and applied~~ applications for a fused product on a  
22 regular grid. Aerosol data assimilation is an operational reality at numerous centers, and like  
23 meteorological reanalyses, aerosol reanalyses will see significant use in the near future. Here

24 we present a standardized 2003 - 2013 global 1x1 degree and 6-hourly modal aerosol optical  
25 thickness (AOT) reanalysis product. This dataset can be applied to basic and applied earth  
26 system science studies of significant aerosol events, aerosol impacts on numerical weather  
27 prediction, and electro-optical propagation and sensor performance, among other uses. This  
28 paper describes the science of how to develop and score an aerosol reanalysis product. This  
29 reanalysis utilizes a modified Navy Aerosol Analysis and Prediction System (NAAPS) at its core  
30 and assimilates quality controlled retrievals of AOT from the Moderate Resolution Imaging  
31 Spectroradiometer (MODIS) on Terra and Aqua and the Multi-angle Imaging SpectroRadiometer  
32 (MISR) on Terra. The aerosol source functions, including dust and smoke, were regionally tuned  
33 to obtain the best match between the model fine and coarse mode AOTs and the Aerosol  
34 Robotic Network (AERONET) AOTs. Other model processes, including deposition, were tuned to  
35 minimize the AOT difference between the model and satellite AOT. Aerosol wet deposition in  
36 the tropics is driven with satellite retrieved precipitation, rather than the model field. The final  
37 reanalyzed fine and coarse mode AOT at ~~550nm~~550 nm is shown to have good agreement with  
38 AERONET observations, with global mean root mean square error around 0.1 for both fine and  
39 coarse mode AOTs. This paper includes a discussion of issues particular to aerosol reanalyses  
40 that make them distinct from standard meteorological reanalyses, considerations for extending  
41 such a reanalysis outside of the NASA A-Train era, and examples of how the aerosol reanalysis  
42 can be applied or fused with other model or remote sensing products. Finally, the reanalysis is  
43 evaluated in comparison with other available studies of aerosol trends, and the implications of  
44 this comparison are discussed.

45 **1.0 Introduction**

46 The importance of aerosol particles in the atmosphere and climate system is recognized across the  
47 earth sciences. Long implicated in climate change investigations (e.g., IPCC 2007; 2013), aerosol  
48 particles influence countless other aspects of science and society. Obvious impacts include biologic and  
49 visual air quality, including health outcomes (Laden et al., 2000; Kappos, et al., 2004), defense  
50 operations, and transportation (Wilkinson et al., 2012). Further, aerosol particles interfere with many  
51 aspects of earth system surveillance, such retrievals of sea surface temperature (e.g., May et al., 1992;  
52 Reynolds, 1989; Robock, 1989) and ocean color (e.g., Gordon, 1997) and land use systems (Song et al.,  
53 2001). Aerosols can also affect atmospheric retrievals or radiances used to constrain temperature,  
54 water vapor, and CO<sub>2</sub> in numerical weather prediction models (Houweling et al., 2005). In all of the  
55 above cases, contiguous spatial and temporal sampling of aerosol loadings is critical. Monitoring  
56 solutions using satellite data alone must cope with variable orbits (polar, high inclination or  
57 geostationary) and sampling times. Based on this large basic applied science need, there is considerable  
58 demand for consistent gridded aerosol products constructed for numerous applications.

59 To meet aerosol monitoring requirements, the climate and earth systems science community has  
60 historically presented aerosol data as either a free-running model (with the advantage of regularly  
61 gridded and timed products, e.g., Tanaka et al., 2003; Miller et al., 2006; Morcrette et al., 2009; Colarco  
62 et al., 2010; Pérez et al., 2011), or irregularly-timed and located satellite data (e.g., Mishchenko et al.,  
63 1999; Torres et al., 2002; Hsu et al., 2004; Levy et al., 2010; Kahn et al., 2010). In both cases, the  
64 products are underdetermined. Models have poorly-resolved emissions, evolution, and sinks, and can be  
65 affected by errors in the underlying meteorological model, whereas satellite data has limited coverage  
66 and underdetermined retrievals based on assumptions that lead to a series of spatially and temporally-  
67 correlated biases (e.g., Shi et al., 2011a). Ultimately, models and remote sensing products present

68 different aspects of atmospheric characteristics. When model and satellite products are compared,  
69 contextual and sampling biases appear (e.g., Zhang and Reid, 2009). For daily and more rapid analysis,  
70 such as for many specific earth system science process study questions or intersensor correction,  
71 neither approach can adequately represent the full state of the aerosol system.

72 To bridge modeling and remote sensing data sources, numerous operational numerical weather  
73 prediction centers have embarked on sophisticated aerosol data assimilation efforts of both passive and  
74 lidar satellite sensors (e.g., Collins et al., 2001; Weaver et al., 2007; Zhang et al., 2008, 2011; Benedetti et  
75 al., 2009; Sekiyama et al., 2010). Satellite products are screened, empirically corrected and assimilated  
76 into models to provide systematic best-available analyses of the aerosol environment. The next step in  
77 this process is to develop best-available reanalyses for community use. Just as meteorological reanalysis  
78 such as the NCAR/NCEP (eg., Kalnay et al., 1996) and ECMWF (eg., Uppala et al., 2005; Dee et al., 2011)  
79 are commonly applied for meteorological applications, aerosol reanalyses are likely to be destined to be  
80 useful data sources for initial analysis or systematic global studies for aerosol sciences.

81 Like meteorological reanalyses, aerosol reanalyses are generated through a rerun of a model that  
82 assimilates historical observational data. Aerosol reanalyses aim to be a best-available, contiguous,  
83 gridded product with consistent temporal reporting. It combines advantages of data accuracy from  
84 satellite products and data consistency from modelling. The data should have good spatial and temporal  
85 coverage and be easy to use. But an aerosol reanalysis is not simply just a rerunning of the model with  
86 aerosol data assimilation. First, strict quality assurance and quality control processes need to be applied  
87 to the satellite data that goes into an assimilation system, such that the model input is as consistent as  
88 possible over the reanalysis period. Biased retrievals in the data assimilation system could result in  
89 erroneous features that can propagate in the short term. Lack of consistency in the model or data can  
90 lead to artifacts that could be mistaken for climatological trends or spurious aerosol events. Second,

91 the performance of the underlying aerosol forward model should be optimized to its upper limit through  
92 a series of tunings to the aerosol sources and wet/dry removal processes. This helps to avoid large and  
93 frequent corrections via the data assimilation cycle, so that the natural model field is as close as possible  
94 to the satellite product and the final reanalysis product is smooth and fluent in space and time.

95 In this paper, we present the Naval Research Laboratory's development of an aerosol reanalysis  
96 product for applied science use through the assimilation of NASA Terra and A-train satellite sensors into  
97 the Navy Aerosol Analysis and Prediction System (NAAPS). The goal is to provide a best available AOT  
98 product for applications that require this parameter. As the system develops and verification datasets  
99 become available, the publically-released analysis will include many other aspects of the aerosol system,  
100 including three dimensional concentrations and radiative effects such as fluxes and heating rates. Our  
101 goals for the initial development of the NAAPS reanalysis and this paper are threefold.

- 102 a) *Development of a baseline applications dataset:* NAAPS has always been operationally focused,  
103 with frequent operational transitions. In support of basic research and climatology applications,  
104 however, the NAAPS model often requires re-runs with updated parameterizations. With  
105 individual case studies being examined dozens of times per year, we wish to support such  
106 endeavors by developing an accurate AOT product that is consistent in quality and time.
- 107 b) *Development of a baseline verification dataset:* Any application of the baseline dataset will  
108 require a comprehensive description of the NAAPS model when run in reanalysis mode, and  
109 how this differs from the operational version of NAAPS. The methods and data for characterizing  
110 the reanalysis performance must be carefully examined and documented.
- 111 c) *Development of a framework for future development:* We wish to investigate the degree a  
112 reanalysis represents the true atmospheric state and the extent that it can be used to study  
113 climatologically-relevant aerosol features like trend and radiative impacts. As more satellite



114 products mature, they can also be incorporated into the reanalysis. The analysis presented here  
115 is intended to be a template for characterization of future reanalysis datasets as they become  
116 available.

117 While the aerosol system is a highly complex internal mixture of anthropogenic, biogenic, open  
118 burning and wind driven emissions, ultimately it is AOT and its simple partition into fine and coarse  
119 mode contributions that we can actually measure and verify globally. Reanalyses on atmospheric gas  
120 composition and/or aerosols are also in development at ECMWF (Inness et al., 2013) and NASA (Buchard  
121 et al., 2015). The aerosol models used for generating these reanalyses are independent in their  
122 underlying meteorology, as well as aerosol sources, sinks, microphysics and chemistry. The AOT  
123 assimilation methodologies, the observed AOT data to be assimilated, and the pre-assimilation  
124 treatments of input data are also different. Validation of multivariate reanalyses of atmospheric  
125 composition is a very complex task, and a comprehensive evaluation is needed. This study focuses  
126 exclusively on the development and validation of a ~~550nm~~550 nm modal (fine mode, coarse mode and  
127 total) AOT reanalysis.

128 In this paper, we provide an up-to-date description of the primary NAAPS model, noting differences  
129 between the reanalysis and operational versions. Our emphasis is on the development of a modal  
130 NAAPS AOT analysis. We describe the methods used to tune modeled aerosol processes. The data  
131 assimilation system used to fuse the model and observations is described, as well as the satellite data  
132 products used in the reanalysis. This is followed by a basic description of the reanalyzed global fine and  
133 coarse mode ~~550nm~~550 nm AOT fields and their verification. We conclude with a brief synopsis and  
134 discussion of our findings. We provide documentation of strengths and pitfalls of reanalysis products  
135 including advice on interpreting like products. For example, we discuss how the data assimilation system  
136 affects diurnal aerosol representation or how long term trends are represented in the simulation that

137 has static industrial emissions. We also discuss the difficulty in keeping meteorological input consistent  
138 at decadal levels. We conclude with a project synopsis and outlook for future experiments.

139

## 140 **2.0 Description of Model: NAAPS and NAVDAS-AOT**

141 The foundation of this AOT reanalysis is the Navy Aerosol Analysis and Prediction System (NAAPS)  
142 and its associated aerosol data assimilation components. NAAPS is an offline aerosol transport model,  
143 which has seen wide use in the community for global aerosol lifecycle research, contextual information,  
144 field mission planning, and operations.

145 The original NAAPS model was based on the Danish Eulerian Hemispheric Model (Christensen,  
146 1997), although since then there have been a number of upgrades to model advection and microphysics.  
147 NAAPS has been run quasi-operationally at NRL since 1998, and became the world's first operational  
148 global aerosol model in 2006 with implementation at the Fleet Numerical Meteorology and  
149 Oceanography Center (FNMOC). The Navy Atmospheric Variational Data Assimilation System (NAVDAS)  
150 for Aerosol Optical Thickness (NAVDAS-AOT; Zhang et al., 2008) was operationally implemented in 2010.  
151 The system assimilates quality assured and quality controlled 2-dimensional MODIS AOT at 550 nm. In  
152 its current operational configuration, NAAPS makes 6-day forecasts, 4 times a day at 1080x540 global  
153 (1/3 degree) spatial resolution and 42 vertical levels driven by truncated T425L60 resolution Navy Global  
154 Environmental Model (NAVGEM) meteorology (Hogan et al., 2014). Papers describing the development  
155 of the operational NAAPS include Witek et al. (2007) for sea salt, Reid et al. (2009) for biomass burning  
156 smoke and Westphal et al. (2009) for dust. Updates to the operational model can be found at  
157 <http://www.nrlmry.navy.mil/aerosol/>.

158 In converting NAAPS from a forecast model to a reanalysis system for the A-train 2003-2013  
159 time period, we desire a system that is consistent spatially and temporally in time and fits within our  
160 computational constraints. This requires, at times, significant departures from the operational model,

161 and some reduction in resolution. In this section, we describe the NAAPS model configured for  
162 reanalysis mode, its AOT assimilation package and the associated MODIS, MISR and precipitation  
163 satellite data used to initialize and assimilate into the model. We also describe the tuning processes  
164 necessary to help ensure spatial and temporal consistency within the reanalysis period.

## 165 2.1 Meteorology fields

166 The current operational version of NAAPS is driven by NAVGEM (Hogan et al., 2014), a global  
167 T425L60 spectral model that is only available since September 2013. The NAAPS reanalysis described in  
168 this paper is driven by the recently-decommissioned Navy Operational Global Atmospheric Prediction  
169 System (NOGAPS) analysis fields for 2003-2013. A full NAVGEM reanalysis is under construction that will  
170 allow higher horizontal and vertical resolution to better constrain future runs of the reanalysis. The  
171 NOGAPS model is a global model that is spectral horizontally and energy-conserving finite-difference  
172 (sigma coordinate) in the vertical (Hogan and Rosmond, 1991; Hogan and Brody, 1993). Four times a day,  
173 the weather forecast models provide 6-day forecasts of the dynamical and surface analysis fields to  
174 NAAPS at 3-hr intervals. The reanalysis uses only the 00, 06, 12, and 18Z analyses with the associated 3-  
175 hr forecast fields to make up the 3-hr time series of dynamical forcing. NOGAPS variables used by  
176 NAAPS are the topography, sea ice, surface stress, surface heat flux, surface moisture flux, surface  
177 temperature, surface wetness, snow cover, stratiform precipitation, convective precipitation, lifting  
178 condensation level, cumulus fractional coverage, cumulus cloud height, surface pressure, three  
179 components of the wind, temperature, and relative humidity. For data assimilation, NOGAPS uses the  
180 NRL Atmospheric Variational Data Assimilation System (NAVDAS), which is still used operationally for  
181 assimilation of a large variety of conventional and satellite-based observations (Daley et al., 2001). While  
182 NOGAPS has had some resolution changes over the 2003-2013 study period (ranging from T159 to T319),

183 spectrally truncated NOGAPS meteorology data is incorporated into the NAAPS reanalysis for each 6  
184 hour time step at the prescribed 1x1 degree resolution.

185 As the primary sink of aerosol particles, the precipitation component of NOGAPS is worth special  
186 attention. Often in large scale models the parametrized precipitation schemes for tropical regimes  
187 generate widespread light precipitation, while the long-term total precipitation amount is comparable  
188 to observations (Dai, 2006, Sun et al., 2007). Similarly, global models also have difficulty placing  
189 significant convective cells, particularly moderately-sized squall lines or coastal thunderstorms. Diurnal  
190 precipitation cycles are also poorly represented by numerical models. These characteristics of model  
191 precipitation are shown to affect removal of aerosol particles and can have significant impact on  
192 regional AOT simulations (Wilcox and Ramanathan, 2004; Xian et al., 2009). For the reanalysis, tropical  
193 precipitation from NOAA Climate Prediction Center (CPC) MORPHing technique (CMORPH, Joyce et al.,  
194 2004) is used whenever available to improve aerosol wet deposition in the manner described in Xian et  
195 al. (2009), in which cloud structure from the model is retained but precipitation flux is changed  
196 accordingly. CMORPH combines infrared (IR) and passive microwave data (PMW) retrieved from  
197 instruments onboard multiple geostationary and lower-orbiter satellites. CMORPH was chosen for this  
198 role as it appears to have the best representation of temporal and spatial patterns of tropical  
199 precipitation among satellite precipitation products (Janowiak et. al, 2005; Sapiano and Arkin, 2009).

200

## 201 2.2 Aerosol Model

202 As noted above, NAAPS is a global aerosol model originated in the mid-1990's from a  
203 hemispheric sulfate chemistry model developed by Christensen (1997). Dust, sea salt and smoke have  
204 been added to the original model, and are documented in Westphal et al. (2009), Witek et al. (2007)  
205 and Reid et al. (2009), respectively. Given that what is commonly referred to as regional pollution or

206 haze is a result of complex anthropogenic and biogenic emissions and chemistry, here we replaced the  
 207 simplified Christensen (1997) SO<sub>2</sub> and sulfate chemistry. As elaborated in Section 2.2.6, anthropogenic  
 208 SO<sub>2</sub>, sulfate and organics, are combined with biogenic emissions to form an anthropogenic and biogenic  
 209 fine (ABF) aerosol particle species.

### 210 2.2.1 Aerosol Model Dynamics

211 The equations solved in the model have the form

$$212 \quad \frac{\partial q_i}{\partial t} = - \left( u \frac{\partial q_i}{\partial x} + v \frac{\partial q_i}{\partial y} + \dot{\sigma} \frac{\partial q_i}{\partial \sigma} \right) + \left( K_x \frac{\partial^2 q_i}{\partial x^2} + K_y \frac{\partial^2 q_i}{\partial y^2} + \frac{\partial(\Gamma^2 K_z \frac{\partial q_i}{\partial \sigma})}{\partial \sigma} \right) + P_i - Q_i \quad , \quad (1)$$

213 where  $q_i$  is the mass mixing ratio (kg kg<sup>-1</sup>) for the species  $i$ ,  $q_i = c_i/\rho$ , where  $c_i$  is the mass concentration  
 214 (kg m<sup>-3</sup>) and  $\rho$  is the density of air (kg m<sup>-3</sup>),  $x$  and  $y$  are the horizontal coordinates ([in meter along](#)  
 215 [longitude and latitude directions](#)),  $\sigma$  is the terrain-following vertical coordinate ( [\$\sigma = p/p\_s\$ , where  \$p\$  is the](#)  
 216 [present pressure and  \$p\_s\$  surface pressure](#)) that ranges from 1 at the surface to 0 at the model top,  $u$ ,  $v$ ,  $\dot{\sigma}$   
 217 are the advection velocity in the  $x$ ,  $y$  and the vertical directions of the  $\sigma$ -coordinates,  $K_x$  and  $K_y$  are  
 218 horizontal diffusion coefficients that are assumed to be constant ( $K_x = K_y = 6 \times 10^4 \text{ m}^2 \text{ s}^{-1}$ ), And  $K_z$  is the  
 219 vertical diffusion coefficient based on the Monin-Obukhov similarity theory for the surface layer  
 220 (Obukhov, 1971). The  $K_z$  profile is extended to the whole boundary layer by using a simple extrapolation  
 221 (Hertel et al., 1995). Finally,  $\Gamma = d\sigma/dz$  (m<sup>-1</sup>).  $P_i$  are the sources and  $Q_i$  are the sinks for the species  $i$ .

222 Equation 1 is solved on a spherical grid with 1° x 1° horizontal resolution and 25 vertical irregular  
 223  $\sigma$ -coordinate levels in the reanalysis product presented here. The average depth of the first layer is ~30  
 224 meters, and consecutive layers gradually increase in depth towards the top layer, which ends at ~18 km  
 225 (70hpa). Advection is calculated using a semi-Lagrangian scheme (Staniforth and Cote, 1991), with  
 226 departure points calculated using the method of Ritchie (1987). Horizontal and vertical diffusion are  
 227 calculated with a finite-element method (e.g., Bathe, 2006).

228 2.2.2 Aerosol Optical Properties in NAAPS

229 Aerosol microphysics are treated relatively simply in NAAPS. This is in response to the  
 230 computational needs of an efficient operational forecast model, its operational requirements (e.g.,  
 231 forecast severe visibility reducing events) and the fact that in comparison with the uncertainties in  
 232 source functions as well as transport meteorology, microphysics is relatively well constrained. Dry mass  
 233 concentrations are forecasted with Equation 1 and AOT for each aerosol species is computed assuming  
 234 an effective particle size with respect to mass. Aerosol particles in NAAPS are treated as external  
 235 mixture of the aforementioned species and do not interact with each other. With these assumptions,  
 236 extinction and AOT can be calculated using bulk values of optical properties that have been derived from  
 237 theory and observations. The calculations for scattering ( $b_{scat}$ ,  $m^{-1}$ ), absorption ( $b_{abs}$ ,  $m^{-1}$ ) and extinction  
 238 coefficients ( $b_{ext}$ ,  $m^{-1}$ ), plus the integrated optical ~~thickness~~ ~~depth~~ ( $\tau$ , unitless) are, respectively

239 
$$b_{scat,i}(\lambda, x, y, \sigma) = c_i(x, y, \sigma) \alpha_{scat,i}(\lambda) f_i[r(x, y, \sigma)] \quad , \quad (2)$$

240 
$$b_{abs,i}(\lambda, x, y, \sigma) = c_i(x, y, \sigma) \alpha_{abs,i}(\lambda) \quad , \quad (3)$$

241 
$$b_{ext,i}(\lambda, x, y, \sigma) = b_{scat,i}(\lambda, x, y, \sigma) + b_{abs,i}(\lambda, x, y, \sigma) \quad , \text{ and } (4)$$

242 
$$\tau_i(\lambda, x, y) = \int_1^0 b_{ext,i}(\lambda, x, y, \sigma) \frac{1}{\Gamma} d\sigma \quad , \quad (5)$$

243 where  $\alpha_{ext}$ ,  $\alpha_{scat}$  and  $\alpha_{abs}$  are the mass extinction, scattering, and absorption efficiencies respectively  
 244 ( $m^2 g^{-1}$ ), and  $f_i$  is a scattering hygroscopic growth factor.

245 The bulk mass extinction, scattering, and absorption efficiencies, along with single scattering  
 246 albedo and asymmetry factor for the four aerosol species at wavelength  $\lambda = 550$  nm are given in Table 1.  
 247 For ABF, dust and sea salt, the values are taken from the optical properties of aerosol and clouds-OPAC  
 248 database (Hess et al., 1994). The chosen coefficients for ABF are weighted towards the more-absorbing  
 249 aerosol particles that are generated by less-developed countries that dominate global aerosol fields

250 (Dubovik et al., 2002). Optical properties for smoke are treated similarly, with both empirical  
251 derivations and theory derived from Reid et al. (2005a, b).

252 The effect of humidity on particle light scattering for each aerosol species is represented by the  
253 [HanelHänel](#) (1976) formulation of the hygroscopic growth factor  $f_i(r)$  (unitless), defined as

$$f_i(r) = \left[ \frac{(1-r)}{(1-r_o)} \right]^{-\gamma_i}, \quad (6)$$

254 where  $r$  is the relative humidity,  $\gamma_i$  is an empirical species-dependent exponent and  $r_o$  is the reference  
255 relative humidity that is set equal to 30%. In NAAPS,  $\gamma_i$  is taken as 0.5 for ABF particles assuming 40%  
256 sulfate and 60% organic aerosols. In comparison,  $\gamma_i$  is 0.63 for sulfate ([HanelHänel](#), 1976), 0.18 for  
257 smoke (Reid et al., 2005b), 0.46 for sea salt (Hegg et al. 2002; Ming and Russell, 2001), and zero for dust  
258 (Li-Jones et al., 2002). A maximum allowed  $r$  is 95%. We assume absorption  $\alpha_{\text{abs}}$  is not affected by  
259 humidity.

### 260 2.2.3 Sink processes in NAAPS

261 Dry deposition to the surface is accounted for through a decrease of the aerosol concentration  
262 in the lowermost model layer, assuming a dry deposition flux

$$263 F_{DDi} = c_{1i} v_{di}, \quad (7)$$

264 where  $c_{1i}$  is the mass concentration ( $\text{kg m}^{-3}$ ) in the first layer above the surface for the species  $i$ , and  $v_{di}$   
265 is the dry deposition velocity, which is a function of aerosol type and surface type.

266 For particle deposition over water, the dry deposition velocity  $v_d$  is set to  $0.0002 \text{ m s}^{-1}$  for  
267 anthropogenic and biogenic fine particles,  $0.0003 \text{ m s}^{-1}$  for smoke loosely following the theoretical  
268 relation between over water  $v_d$  and particle radius in Slinn and Slinn (1980), assuming bulk effective  
269 radius listed in Table 1 for the two types of aerosols.  $v_d$  is set to  $0.001 \text{ m s}^{-1}$  over water for dust particles  
270 after tuning to minimize AOT corrections through the data assimilation process (more details in section

271 2.4.2). Dry deposition of sea salt to open water is given by the formula in Slinn and Slinn (1980),  
272 assuming a dry mass mean radius near 1.5  $\mu\text{m}$ , and written as

$$v_{dss} = C_d U_{10}, \quad (8)$$

273 where  $C_d = 1.3 \times 10^{-3}$  is the drag coefficient, and  $U_{10}$  the wind speed at 10 meters above the sea  
274 surface in  $\text{m s}^{-1}$ .

275 For particle deposition over land, the method of Walcek et al. (1986) is used and the explicit  
276 expression for  $v_d$  is the same as in Christensen (1997; Eq. (9)), which is a function of surface friction  
277 velocity and Monin-Obukhov length, which is a measure of the stability of the surface layer (Obukhov,  
278 1971, Eq. 26). This is written as

$$v_d = \begin{cases} \frac{u_*}{a} \left( 1 + \left( \frac{-300}{L} \right)^{2/3} \right) & \text{for } L < 0 \\ \frac{u_*}{a} & \text{for } L > 0 \end{cases}, \quad (9)$$

279 where  $u_*$  is the surface friction velocity in  $\text{m s}^{-1}$ ,  $a = 500$  (except for a forest with leaves, where  $a = 100$ ),  
280 and  $L$  is the Monin-Obukhov length.  $v_d$  is calculated using Eq. (9) for all the aerosol species in the model.

281 Gravitational settling is also applied to the aerosol particles in the model. Dry deposition is only  
282 applied in the lowermost model layer, whereas gravitational sedimentation takes place within the whole  
283 vertical domain except the lowermost model layer, as it is taken into account in  $v_d$ .

284 The wet deposition of particles is assumed to be similar to that for sulfate aerosol, based on a  
285 simple scavenging ratio formulation (e.g. Iversen, 1989). The scavenging coefficient is calculated in the  
286 same way as in Witek et al. (2007), as a function of the precipitation mass flux with different below-  
287 cloud and in-cloud scavenging ratios, written as



288

$$W(\sigma) = \begin{cases} \frac{\Lambda_{bc} P_a(\sigma)}{H \rho_w} & \text{below cloud scavenging} \\ \frac{\Lambda_c P(\sigma)}{H \rho_w} & \text{in cloud scavenging} \end{cases}, \quad (10)$$

289 where  $P_a(\sigma)$  and  $P(\sigma)$  ( $\text{kg m}^{-2}\text{s}^{-1}$ ) are the total downward flux densities of precipitation mass at a  
 290 given  $\sigma$ -level below or in a precipitating cloud, respectively.  $H$  is an effective thickness for scavenging  
 291 (set to 1000 m),  $\Lambda_{bc} = 1 \times 10^5$  is the below-cloud scavenging ratio,  $\Lambda_c = 7 \times 10^5$  is the in-cloud  
 292 scavenging ratio, and  $\rho_w$  is the density of water.

#### 293 2.2.4 Dust

294 Dust emissions occur whenever the friction velocity exceeds a threshold value, snow depth is  
 295 less than a critical value, and the surface moisture is less than a critical value (Westphal et al., 1988).

296 The dust emission flux follows the equation

$$297 F_{dust} = c e_f u_*^4, \quad (11)$$

298 where  $e_f$  is the erodible fraction of a grid box (unitless),  $u_*$  is the surface friction velocity with the  
 299 threshold value of  $0.6 \text{ m s}^{-1}$  for dust mobility, and  $c$  is a scaling constant of  $4.5 \times 10^{-7} \text{ g m}^{-2} \text{ s}^{-1}$ . In the  
 300 operational version of NAAPS, the erodibility map is empirically derived from the United States  
 301 Geological Survey Land Cover Characteristic Database and Total Ozone Mapping Spectrometer Aerosol  
 302 Index values (Walker et al., 2009). While in general the operational version of NAAPS has good dust  
 303 scores, NAAPS clearly has a high bias for dust for the Sahara. For the reanalysis, the use of Ginoux et al.  
 304 (2001) dust sources mitigated much of this bias. The Ginoux et al. (2001) erodibility map associates dust  
 305 sources with topographic depressions and has many of the same features as seen in Westphal et al.  
 306 (1988), yet its geologic input data tightened individual source areas.

307 Regional source tuning is also applied in the NAAPS reanalysis, which is described in Section 2.4.

308 Dust is emitted into the bottom two layers of the model (below 100m) when friction velocity exceeds  
 309 the threshold and surface wetness is below a critical value (0.4). Then, dust is transported by model

310 dynamics both horizontally and vertically in the boundary layer and the free troposphere. Dust removal  
311 includes sedimentation, dry deposition and wet removal, which is constrained with CMORPH  
312 precipitation within the tropics. Dust is assumed to be totally hydrophobic and hence the hygroscopic  
313 growth factor is set to 1.

#### 314 2.2.5 Sea Salt

315 The sea salt component for operational NAAPS and the NAAPS reanalysis was developed by  
316 Witek et al. (2007). Sea salt emissions are driven dynamically by sea surface wind. The sea salt dry mass  
317 flux  $F_{ssa}$  ( $\text{kg m}^{-2}\text{s}^{-1}$ ) from the surface is based on the whitecap method and the Monahan's formulation of  
318 the source function (Monahan et al., 1986), and has the empirical form

$$F_{ssa} = a_s U_{10}^{b_s} \quad , (12)$$

319 where  $U_{10}$  is the wind speed at 10 meters above the sea surface in  $\text{m s}^{-1}$ ,  $a_s = 1.37 \times 10^{-13}$  and  $b_s = 3.41$   
320 for particles with diameters from 1.6 to 16  $\mu\text{m}$ .

321 Dry deposition of sea salt over water is proportional to the sea surface wind speed, following Slinn and  
322 Slinn (1980) and over land follows Eq. (9). Sea salt particles are assumed to undergo hygroscopic growth  
323 depending on ambient atmospheric relative humidity, following the growth rate shown in Eq. (6). Sea  
324 salt scattering coefficient is based on swelled particles, while absorption coefficient is assumed not  
325 effected by the swell.

#### 326 2.2.6 Anthropogenic and biogenic fine particles (ABF)

327 The most significant change to NAAPS microphysics for the reanalysis is the development of a  
328 method to account for complex anthropogenic and biogenic species while not significantly increasing  
329 the computational cost of the model. Originally, the only anthropogenic emissions and predictive  
330 variables within NAAPS were  $\text{SO}_2$  and sulfate. However, organic species constitute one of the most  
331 important contributors to the mass of atmospheric aerosols (Zhang et al., 2007, Jimenez et al., 2009),  
332 and indeed commonly dominate the submicron aerosol mass and AOT. This organic aerosol mass, while

Formatted: Line spacing: 1.5 lines

333 having a significant component attributable to primary organic aerosol (POA) emission, is predominantly  
334 secondary organic aerosol (SOA; i.e., created in the atmosphere from volatile organic carbon (VOC)  
335 precursors in the gas phase, such as, isoprene, terpenes and aromatics; e.g., Zhang et al, 2007). These  
336 precursors are largely biogenic in origin. Ultimately, the complex chemical interactions between  
337 anthropogenic and biogenic emissions result in a photochemical soup that cannot be directly linked to a  
338 single origin.

339 For realistic simulation of AOT, primary and secondary organic aerosols must both be included in  
340 the NAAPS model in some form. To be consistent with the NAAPS reanalysis' philosophy of simple and  
341 tractable physics, the sulfur-related species has been replaced with a bulk anthropogenic and biogenic  
342 fine (ABF) mass category to account for the entire class of anthropogenic and biogenic emissions and  
343 their secondary particle products. This species class includes all accumulation mode particles, including  
344 biogenic marine, outside of open biomass burning, as described in Section 2.2.7. The first component of  
345 this mixture is the original sulfur chemistry. Sulfate aerosols are produced by chemical processes in the  
346 atmosphere from gaseous precursors, mainly sulfur dioxide (SO<sub>2</sub>) from anthropogenic sources and  
347 dimethylsulfide (DMS) from biogenic sources. For NAAPS reanalysis, SO<sub>2</sub> emissions are updated from  
348 GEIA Version 1A (i.e., 1985) (Benkovitz, 1996) to Monitoring Atmospheric Composition &  
349 Climate/CityZen EU projects (MACCity) inventory 2005-2010 average (Granier et al., 2011, Diehl et al.,  
350 2012), which reflects the increased emission in India and China over the past decade and also includes  
351 monthly variation. DMS emission fluxes at the air-sea interface are computed using the Saltzman (1993)  
352 parameterization, with the monthly DMS seawater concentrations from Lana et al. (2011). DMS are  
353 immediately converted to 95% sulfur dioxide and 5% sulfate in the model. SO<sub>2</sub> chemistry follows  
354 Hoffmann and Calvert (1985), in which oxidation of sulfur solution (S(IV)) by hydrogen peroxide (H<sub>2</sub>O<sub>2</sub>)  
355 and dissolved ozone (O<sub>3</sub>) are considered climatologically. We assume background oxidants H<sub>2</sub>O<sub>2</sub> and O<sub>3</sub>

356 are not depleted by reactions. Ultimately, sulfur chemistry accounts for roughly one half of all non-  
357 biomass burning fine mode AOT.

358 Inclusion of POA in the NAAPS reanalysis is straightforward, including the major VOC species  
359 that act as precursors for the SOA. We apply the 2005-2010 monthly-mean MACCity data base for  
360 anthropogenic (industrial and transport) emissions of POA and SOA precursors (Granier et al., 2011), the  
361 Bond et al (2004) biofuels data with a monthly scaling factor based on Jeong (2011), and the Precursors  
362 of Ozone and their Effects in the Troposphere (POET) climatological monthly emissions inventory for  
363 biogenic VOC's (Olivier et al., 2003). For the actual SOA formation process, the Volatility Basis Set (VBS)  
364 approach has been adopted (Donahue et al., 2006; Ahmadov et al., 2012). This greatly reduces both the  
365 number of necessary precursor species and the number of SOA products from the vast numbers needed  
366 to explicit represent SOA formation and evolution by formulating the conversion process in terms of a  
367 limited number of precursor species and volatility classes (four in our case) for the reaction products.  
368 The reaction yields for the various VBS classes, upon which the approach ultimately depends, are  
369 derived from numerous chamber studies as cited, for example, in Ahmadov et al. (2012) and Donahue et  
370 al. (2006). Phase partitioning is done as per Pankow (1994).

371 To further simplify the inclusion of organic aerosols in the NAAPS model, both the POA and SOA  
372 are calculated in a "preprocessor" at model initialization. For the SOA, this includes calculation of the  
373 yield of SOA product mass from the emissions inventory VOC's, based on the VBS model, and the  
374 treatment of this mass as a primary aerosol emission, similar to the POA. Utilizing the similarity in  
375 microphysical and optical properties of OA and sulfate, the model carries POA and SOA together with  
376 sulfate as aforementioned "anthropogenic and biogenic fine". This approach has some obvious  
377 shortcomings, but it carries minimal computational cost and has much improved the simulation of AOT,  
378 especially the model bias and correlation with AERONET over India, China and Eastern United States.

379 2.2.7 Biomass Burning Smoke

380 Biomass burning has a wide coverage globally, from the tropics to the high latitudes, and it  
381 significantly impacts the total light absorption budget (Bond et al., 2013). Unlike other aerosol sources  
382 that are meteorologically driven (e.g., dust and sea salt) or prescribed in a seasonal or monthly inventory  
383 (e.g., pollution), smoke emissions have significant variability that hinders easy parameterization.  
384 Configuring the NAAPS model with biomass burning aerosols as a separate species permits explicit  
385 hypothesis testing about the sources, sinks, and optical properties of these aerosols. Operational NAAPS  
386 has adopted the satellite active fire hotspot based approach through the Fire Locating and Modeling of  
387 Burning Emissions (FLAMBE1.0; Reid et al., 2009; Hyer et al., 2013). The model converts the smoke  
388 emission to total mass injected by multiplying by the fire size. This value is then divided by the area of  
389 the grid cell and the fire duration to create a flux as an hourly input to the model. FLAMBE can use  
390 satellite fire products from either geostationary sensors, which offer faster refresh rates and  
391 observation of the full diurnal cycle, or polar orbiters, which have greater sensitivity. Polar orbiting  
392 satellites have significant biases not only in their daily sampling pattern, but also additional artifacts  
393 from day to day shifts in the orbital pattern (e.g., Heald et al., 2003, Hyer et al., 2013). Over the  
394 reanalysis period, multiple changes in the geostationary constellation posed a challenge for consistency  
395 of the smoke source function. Therefore, a polar-only version of FLAMBE was created for the reanalysis.

396 Given that the NAAPS reanalysis coincides with the NASA EOS system, MODIS-based fire  
397 products and emissions are applied. MODIS orbits have a 16-day repeat cycle, with daily coverage of the  
398 globe excepting small gaps between orbits at the equator. Areas that are not covered one day are  
399 centered on the orbit the next. The Fire Inventory from NCAR (FINN, Wiedinmyer et al. 2011), which is  
400 also based on MODIS active fire detections, uses a 3-day moving average to account for gaps and orbital  
401 variations. After testing multiple coverage corrections, we found that for the reanalysis a simple two-day  
402 maximum (previous day and present day) fire signal largely mitigated orbital effects and thick clouds in a

403 tractable way. This correction is consistent with the self-sustained nature of regional fire emissions, and  
404 further improves upon the scores presented in Reid et al. (2009).

405 Smoke injection height combined with boundary layer mixing has a strong influence on how  
406 smoke is dispersed. Most plumes are observed as constrained within the planetary boundary layers,  
407 especially within the tropics and subtropics (Tosca et al., 2011, Campbell et al., 2013). Large boreal fires  
408 can pump smoke to higher altitudes, though these fires constitute only a very small portion of the total  
409 fires and global budget of AOT (Fromm and Servranckx, 2003; Kahn et al., 2008). In NAAPS, smoke is  
410 injected into the bottom four layers of the model, which is approximately the bottom 400 m of the  
411 model. Tuning of injection height to match observed aerosol vertical profiles is feasible in regional  
412 studies (e.g., Wang, et al., 2013). However, we use the uniform injection height in NAAPS, considering  
413 that boundary layer processes generally quickly mix aerosols well within the boundary layer or below  
414 the models significant inversion height to produce a result similar to the observations of Kahn et al.  
415 (2008).

416

### 417 2.3 AOT assimilation

418 The core of the NAAPS AOT reanalysis is AOT assimilation using the Navy Atmospheric  
419 Variational Data Assimilation System for Aerosol Optical Thickness (NAVDAS-AOT; Zhang et al., 2008).  
420 NAVDAS-AOT is a system that, by default, assimilates quality-controlled two-dimensional MODIS AOT at  
421 550 nm into NAAPS. It additionally has the ability to perform three-Dimensional (3DVAR) assimilation  
422 using the Cloud Aerosol Lidar with Orthogonal Polarization (CALIOP) product of Campbell et al. (2010) in  
423 Zhang et al. (2011). The main impact of 3DVAR assimilation is redistribution of aerosol mass vertically,  
424 while conserving the total column mass and AOT. CALIOP data is available for only part (2006-2013) of  
425 the reanalysis period, therefore, in this first study we perform 2DVAR AOT assimilation only.

426

427 2.3.1 Formulation of NAVDAS-AOT

428 The NAAPS prognostic variable is the 3D aerosol mass concentration. A 2DVAR approach is  
429 adopted for AOT assimilation simply because AOT retrievals from MODIS and MISR are a column-  
430 integrated aerosol optical property. The 2DVAR AOT assimilation is realized through three steps:

431 (1) Convert NAAPS mass concentration AOT:

$$\tau_{b\lambda} = H_{m_\tau}(C_m) + \epsilon_{b\lambda} \quad , (13)$$

432 where  $\tau_{b\lambda}$  is the background (prior analysis) AOT vector,  $C_m$  is the NAAPS mass concentration, and  $H_{m_\tau}$  is  
433 the forward operator that represents the conversion of NAAPS mass concentration to AOT.  $\epsilon_{b\lambda}$  is the  
434 error in  $\tau_{b\lambda}$  introduced by the  $H_{m_\tau}$  operator;

435 (2) 2-D variational assimilation of the AOT field:

$$\tau_{a\lambda} = \tau_{b\lambda} + P_b H^T [H P_b H^T + R]^{-1} [\tau_{o\lambda} - H(\tau_{b\lambda})] \quad , (14)$$

436 where  $\tau_{a\lambda}$  is the analysis AOT vectors,  $\tau_{o\lambda}$  is the observation AOT vector, and H is the observation  
437 operator that represents any necessary spatial and temporal interpolations from the background to  
438 observational space.  $P_b$  and R are the background error covariance and observational error covariance  
439 matrices, respectively. The analysis field can be considered as the background ( $\tau_{b\lambda}$ ) plus a correction  
440 term (the second term on the right hand side of Eq. 14), which is the difference between the  
441 observation and background vectors weighted by the ratio of background error covariance matrix to  
442 total error covariance matrix in the observational space;

443 (3) Convert the analysis AOT vectors to NAAPS mass concentration:

$$C_m = H_{\tau_m}(\tau_{a\lambda}) + \epsilon_m \quad , (15)$$

444 where  $H_{\tau_m}$  is the backward operator that performs the conversions from AOT to NAAPS mass  
445 concentration. In the backward operation, a scaling factor is applied to the vertical profile of aerosol  
446 mass based on the ratio of the AOT correction and background AOT, while keeping the hygroscopic

447 growth rate (Eq. 6) unchanged.  $\varepsilon_m$  is the error in  $C_m$  introduced by the  $H_{\tau_m}$  operator. Both  $\varepsilon_m$  and  $\varepsilon_{b\lambda}$  can  
448 be transformed as part of the error term of  $\tau_{b\lambda}$ , which is assumed to be zero for this study.

449

### 450 2.3.2 Observational and background model error covariance matrices

451 Both observational and model errors could contain systematic bias, either of which could be  
452 removed or minimized through pre-processing. For example, our quality assurance (QA) and quality  
453 control (QC) methodology (Section 2.3.3) attempts to remove systematic bias as much as possible from  
454 the AOT observations. Likewise the tuning process described in Section 2.4 attempts to remove  
455 systematic bias from the model background. Thus, both model background and observations are  
456 assumed to be unbiased in NAVDAS-AOT.

457 In NAVDAS-AOT, observational errors are assumed to be uncorrelated. Thus, only  
458 observational error variances are needed. The error variances for the gridded satellite AOT data are  
459 computed by the summation of instrumental error variances and sample error variances (Zhang et  
460 al., 2008). The instrumental error variance is estimated through the comparison of satellite and  
461 ground-based sun-photometer data as shown in Zhang and Reid (2006) and Shi et al., (2011a) for MODIS  
462 “Dark Target”, and Shi et al., (2014) for MISR aerosol products. The sample error variance measures the  
463 variance in the gridded mean (or the representative error variance). For a  $1^\circ$  latitude by  $1^\circ$  longitude grid,  
464 the sample error variance is derived by the spatial variance of the AOT data of the grid divided by the  
465 number of observations that are used in computing the gridded mean value.

466 The background error covariance is computed for any given two horizontal model grids locations  
467  $m$  and  $n$  based on the following equation

468 
$$P_b^{mn} = [S_b^m]^{1/2} C_b^{-1/2} [S_b^n]^{1/2}, \quad (16)$$

Formatted: Font: Italic

Formatted: Font: Italic



469 where  $P_b^{mm}$  is the background error variance for horizontal grid locations of  $m$  and  $n$ .  $S_b^m$  and  $S_b^n$  are  
 470 the model error variances at grid locations  $m$  and  $n$ , respectively.  $C_b$  is the horizontal background error  
 471 correlation between the two grid locations. Similar to observational error variances, model error  
 472 variances are also estimated using ground based sun-photometer data, and the values are reported in  
 473 Zhang et al., (2008). The  $C_b$  values are computed using the second order auto-regressive (SOAR)  
 474 approximation (Daley and Barker, 2001),

$$475 \quad C_b(m, n) = (1 + R_{mn} / L) \exp(-R_{mn} / L) \quad . (17)$$

476 Here  $R_{mn}$  is the great circle distance between  $m$  and  $n$ .  $L$  is the horizontal error correlation length. The  
 477 horizontal error correlation length is estimated through evaluating the differences in AOT between  
 478 satellite observations and 6-hour model forecasts as a function of horizontal distance.  $L$  is set to 200 km  
 479 for this study based on Zhang et al., (2008).

480

### 481 2.3.3 Input data for NAVDAS-AOT and its preprocessing treatment

482 The basis of input data for the reanalysis is operational MODIS Collection 5 AOT (Levy et al.,  
 483 2007; 2010; Remer et al., 2005; 2008) and Multi-angle Imaging SpectroRadiometer (MISR) AOT products  
 484 (Martonchik et al., 2009, Kahn et al., 2009, Kahn et al., 2010). MODIS Deep Blue for Collection 5 is not  
 485 used here due to bias issues, but it is expected that improvements in Collection 6 will be made and the  
 486 data could be assimilated (Shi et al., 2013). Extensive quality assurance (QA) and quality control (QC)  
 487 procedures applied to the MODIS C5 AOT are conducted as described in Zhang et al. (2006) and Shi et al.  
 488 (2011a) for over water and Hyer et al. (2011) for over land. These QA/QC procedures are especially  
 489 important for this application, because the analysis must be heavily weighted to the observations to  
 490 allow assimilation for correct for errors such as missing dust and smoke sources. Under these

Formatted: Font: Italic

Formatted: Font: Italic

Formatted: Font: Italic

Formatted: Font: Italic

Formatted: Font: Italic

Formatted: Font: Italic

Formatted: Font: Italic

Formatted: Font: Italic

491 circumstances, the impact of noisy data is large and proper filtering and correction of data is critical.  
492 QA/QC procedures implemented for MODIS and MISR AOT include a) strict checks for removal of  
493 possible cloud contamination, b) corrections for the lower boundary condition, such as wind speed to  
494 correct for white caps and specular reflection over water and surface albedo over land, and c) aerosol  
495 micro-physical corrections based on derived fine mode fraction over water and regionally over land. This  
496 strict quality assuring and quality control procedure is necessary to remove outliers and minimize  
497 erroneous aerosol features in MODIS that would adversely impact the model and propagate through the  
498 system. Currently, the total global data loss through screening of MODIS is about 40%, with a reduction  
499 of absolute errors of 10–30% over water (Zhang et al., 2006; Shi et al., 2011a). Over-land, the QA/QC  
500 procedures reduce data volume by ~60% and improve the global fraction of MODIS AOT within  $0.05 \pm 20\%$   
501 of AERONET (Hyer et al., 2011). The data are aggregated into a  $1^\circ \times 1^\circ$  grid that matches the model  
502 resolution where additional buddy checks are applied.

503         A benefit of a reanalysis is that observations that are not timely enough to be incorporated into  
504 an operational run can be utilized. Thus, while MODIS products are used in all versions of NAAPS, for the  
505 reanalysis we can make use of MISR. Though narrower in swath than MODIS, and thus providing less  
506 relative coverage, MISR has two key benefits. First, MISR is on Terra and its imaging swath is in the  
507 MODIS sun-glint region. Hence, MODIS plus MISR completes the MODIS swath with full coverage.  
508 Second, the MISR over-land algorithm has an advantage over retrievals conducted with other sensors in  
509 its handling of the lower boundary condition, provided that  $AOT < 0.8$ . In particular, there are large  
510 spatially-correlated discrepancies between the retrieved MODIS and MISR AOT in regions of high albedo  
511 as a result of deficiencies in the MODIS lower boundary condition (Shi et al., 2011b). Notable regions of  
512 discrepancy between MODIS and MISR include the Andes Mountains, Saharan Africa, the Arabian  
513 Peninsula and Central Asia (Shi et al., 2011b). Further, MISR can retrieve AOT in desert region at high  
514 efficacy where the operational MODIS Collection 5 “Dark Target” products cannot, thus providing

515 further coverage in desert regions. Quality-assuring (QA) and quality control (QC) procedures, including  
516 the use of MODIS cloud mask products to reduce cloud contamination in MISR data sets and applying  
517 various quality checks and empirical corrections on MISR Level 2 aerosol products, are conducted to  
518 generate data assimilation (DA) quality data sets (Shi et al., 2011c, 2014). Then the data are aggregated  
519 into a 1° latitude by 1° longitude grid.

520 Data assimilation using NAVDAS-AOT is used to produce a new analysis after every six hours of  
521 NAAPS integration time. The MODIS and MISR Level 2 aerosol products are typically acquired in a 6-hr  
522 range centered on the nominal valid time of the analysis (i.e., 0, 6, 12 and 18 UTC) from NASA data  
523 servers. Then QA/QC processes convert MODIS and MISR level 2 data into filtered, corrected, and  
524 aggregated AOT observations with associated uncertainty estimates for assimilation in NAVDAS-AOT.  
525 After QA/QC processes, the general pattern of data coverage from MODIS and MISR for each  
526 assimilation cycle is shown in Fig. 1. The observed geographic pattern is attributed to the fact that  
527 MODIS and MISR AOT retrievals are limited to daytime and a limited range of sun-sensor geometries.  
528 The longitudinal range for which MODIS and MISR data is available in a given assimilation cycle is limited  
529 because Terra and Aqua are in sun-synchronous orbits with equatorial overpass time of 10:30 and 13:30  
530 local solar time, respectively.

531 For the MODIS sensors, overlapping coverage between Terra and Aqua over the 6-hr data  
532 acquisition period does occur and a mean of Terra and Aqua weighted to the number of Level 2  
533 retrievals from each sensor. The contribution of each individual sensor to the total volume of the MODIS  
534 DA quality data is about 50% on average, although this number is highly variable on the ~~6-hrly~~6-hourly  
535 basis, with the variability depending on the observability of the sensors (e.g., cloudy vs. non-cloudy, land  
536 vs. ocean, etc...). Because of its narrower swath compared to MODIS, the data volume of the MISR DA-  
537 quality data is only about 22% on average of that of MODIS. Approximately half of the MISR DA-quality

538 | data overlaps with MODIS. When overlapping of MISR and MODIS 1°x1° ~~6-hrly6-hourly~~ DA-quality data  
539 | occurs, the mean of the two is taken for final assimilation purpose.

540 |         The seasonal geographic distribution of the total number of ~~6-hrly6-hourly~~ 1°x1° fused MODIS  
541 | and MISR DA quality AOT data averaged over 2003-2013 is shown in Fig. 2 (left column). Areas with high  
542 | cloud coverage, including the ITCZ and the subtropical stratus cloud deck regions, have relatively less  
543 | data. In the polar regions, cloud contamination often exists in satellite-retrieved AOT data, leading to  
544 | elevated AOTs. The Southern Oceans is an example of cloud-enhanced MODIS AOT, for instance (Toth et  
545 | al., 2013). As a result, high-latitude AOT data are filtered out in the QA/QC process. The cut-off latitudes  
546 | for AOT data to be assimilated are 40°S over water for the southern hemisphere and 80°N for the  
547 | northern hemisphere. In addition, because MODIS and MISR AOT observations are only available during  
548 | daylight, and thus there are no observations during polar nights, this results in more data counts in  
549 | boreal summer than in boreal winter. Fig. 2 also shows that areas with bright desert (e.g., Saharan Africa,  
550 | the Arabian Peninsula and Central Asia), or snowy/icy surfaces (e.g., Andes Mountains, Greenland and  
551 | high latitude in boreal winter) have relatively less data to be assimilated, as these regions are mainly  
552 | filled in by MISR retrievals that have a revisit time of seven days on average rather than a revisit time of  
553 | one day by MODIS.

554 |         The start date of the reanalysis is 1 January 2003, based on the availability of the observational  
555 | data used in the reanalysis. Terra MODIS and MISR AOT data are first available in March, 2000, and Aqua  
556 | MODIS AOT is first available in July 2002. An additional consideration is CMORPH precipitation data,  
557 | which is used to replace model precipitation within the tropics, is not available until December 2002.  
558 | Since the required spin-up time for the aerosol model is one month, the reanalysis starts at 1 January,  
559 | 2003. Figure 3 shows the time evolution of ~~6-hrly6-hourly~~ data counts of the global MODIS, MISR and  
560 | the fused 1°x1° grid DA quality AOT in dots and their center-point thirty-day running average in solid  
561 | lines. Throughout the reanalysis time period (2003-2013), the data counts of the DA quality data are

562 relatively stable, despite small dips in December 2003 in both MISR and MODIS and October 2008 in  
563 MISR due to the upstream data being unavailable. The data count of the fused MODIS and MISR DA  
564 quality data is about 3800 during boreal summer and 2400 during boreal winter, on average. This  
565 essentially follows the seasonal variation of the MODIS DA quality data count, which makes up about 80%  
566 of the total fused MODIS and MISR DA quality data. Half of the remaining 20% is attributed to MISR  
567 alone and half is attributed to the overlapping MISR and MODIS DA quality data. The seasonal variation  
568 of data volume is mainly related to the fact that more AOT data are discarded for the southern  
569 hemisphere high latitudes than the northern hemisphere high latitudes as a result of cloud  
570 contamination, and no observations are available during polar nights (Fig. 2).

571

#### 572 2.4 Tuning studies

573 While AOT data assimilation from sensors such as MODIS and MISR improves NAAPS  
574 performance (Zhang et al., 2014), the natural NAAPS model performance is equally important for  
575 generating a final reanalysis product that aims to match observations. Previous studies have shown that  
576 aerosol source functions, inherent within the natural runs, are one of the largest uncertainties with  
577 respect to aerosol modeling of AOT (e.g., Kinne et al., 2003). As a result, a series of source-tuning  
578 exercises have been carried out on the natural model, using AERONET and satellite AOT observations for  
579 constraint. The tuning exercises consisted of running the model multiple times while iteratively adjusting  
580 model source and sink parameters. Smoke emissions and dust erodibility, for regions as shown in Fig. 4  
581 with some additional divisions as shown in Table S1, were tuned by iterative comparison between  
582 NAAPS model output without data assimilation and AERONET data, as described in Section 2.4.1.  
583 Emissions for some regions not covered by AERONET, as well as aerosol sink parameters, were  
584 constrained using the AOT assimilation correction field as described in Section 2.4.2. A list of the  
585 corrections applied is given in Table S1. The range of variation in optical properties of dry aerosols

586 reported in the literature (e.g., Hess et al., 1998; Kinne et al., 2003) is small compared to other  
587 uncertainties, therefore we adopted the optical properties described in section 2.2.2 without additional  
588 tuning.

#### 589 2.4.1 Tuning of aerosol sources with AERONET

590 The AErosol RObotic NETwork (AERONET, <http://aeronet.gsfc.nasa.gov>), a ground-based global  
591 scale sun photometer network, has been providing high-accuracy measurements of aerosol properties  
592 since the 1990s (Holben et al., 1998; Holben et al., 2001). AERONET instruments measure sun and sky  
593 radiance at several wavelengths, ranging from the near ultraviolet to near infrared during daytime. It is  
594 often used as the primary standard for validating satellite products and model simulations (e.g., Kahn et  
595 al., 2010; Levy et al., 2010; Colarco et al., 2010). Since there are no AERONET data at ~~550nm~~550 nm,  
596 measurements from multiple wavelengths (380 nm to 1020 nm) were used to estimate both fine and  
597 coarse mode AOTs at ~~550nm~~550 nm, based on the Spectral Deconvolution Method (SDA) of O'Neill et al.  
598 (2001, 2003). Extracted fine and coarse mode AOTs from AERONET AOTs are then compared to ABF plus  
599 smoke and sea salt plus dust, respectively. The SDA product has been verified using in situ  
600 measurements (Kaku et al., 2014) and has been shown to be able of capturing the full modal  
601 characteristics of fine and coarse particles while avoiding the uncertainties that come from using static  
602 diameter thresholds, at 0.8 or 1.0  $\mu\text{m}$  for example. Further, the SDA has also been shown to eliminate  
603 any potential cloud bias in fine mode AOTs from AERONET (Chew et al., 2011), although thin cirrus  
604 contamination into the coarse model AOT can still be problematic in some regions such as Southeast  
605 Asia and Equatorial Africa (Chew et al., 2011; Huang et al., 2011).

606 Only cloud-screened, quality-assured Level 2 AERONET data are used in this study (Smirnov et al.,  
607 2000), and the sites are marked with black dots in Fig. 4. Within the reanalysis time period, nearly 600  
608 regular sites provided valid observational data. AERONET Distributed Regional Aerosol Gridded

609 Observation Networks (DRAGON) observations are concentrated over a small area and a short period of  
610 time, and they are excluded from this study to avoid the effect of uneven sampling on the results from  
611 the statistical analysis. Spatially, the 1x1 degree grids in which the AERONET Level 2 data fall within are  
612 identified, and the model AOT is sampled from these identified model grids. Temporally, AERONET Level  
613 2 data are binned into ~~6-hrly~~6-hourly intervals centered at the model synoptic output times of 00, 06, 12  
614 and 18 UTC and then averaged within the bins. The model AOT at ~~550nm~~550 nm is sampled consistently  
615 with AERONET: we extract the model AOT at a site using only times when AERONET had measurements.  
616 A second approach is tested, in which the model data is interpolated onto AERONET observation times.  
617 Validation results from the two methodologies are similar.

618 Empirical regional tuning of smoke and dust emissions is based on the fine and coarse mode  
619 AOT comparisons with AERONET. The globe is divided into sixteen regions, as shown in Fig. 4, each  
620 having their own distinct aerosol characteristics. For example, South America, South Africa, Peninsular  
621 Southeast Asia, and Insular Southeast Asia have a prevailing smoke aerosol species during burning  
622 seasons, while North Africa and Southwest Asia are dust dominated. East Asia and Indian Peninsular  
623 have mixed dust and pollution. Regional emission tuning factors were generated by using the regional  
624 bias and slope of the linear regression between pair-wise NAAPS and AERONET AOT. This is done for  
625 2009-2011 when AERONET data is more abundant than earlier years. Seasonally, data are grouped into  
626 the boreal winter/spring (December to next-May) and boreal summer/fall (June to November) time  
627 periods. These bi-seasonal temporal stratifications account for the major monsoonal and climatic shifts  
628 in the atmosphere while preserving major aerosol seasons such as, for the boreal summer/fall, the  
629 August-October biomass burning seasons in South Africa, South America, and Maritime Continent, the  
630 June-August African dust season, and the U.S. and European summer haze seasons.

631 Regional emission factors, in the form of linear scaling factors applied to the original source  
632 functions for smoke and dust, are derived for each aerosol active season for the three years. For a single

633 tuning factor, it differs slightly from year to year and season to season to a certain range. An average  
634 over the six seasons is taken to generalize this tuning factor for the reanalysis. The model is then run  
635 using the corrected emissions and the results are validated regionally against AERONET to determine  
636 whether the tuning improved bias, correlation, and root mean square error (RMSE). Additionally, the  
637 fine/coarse mode AOT time series of NAAPS and AERONET are reviewed for each site in the region to  
638 ensure the tuning is sensible. This process is repeated iteratively to refine the tuning. In the  
639 supplemental Table 1, the values of the regional multipliers for smoke emission based on the two-day  
640 maximum MODIS-only FLAMBE data base are listed. Also provided are the regional multipliers for soil  
641 erodibility, which are used to modify the dust source (Ginoux et al., 2001). The tuning factor for soil  
642 erodibility changes twice over the 11 years to accommodate the land surface parameterization changes  
643 in the meteorological analysis.

644

#### 645 2.4.2 Tuning with AOT assimilation correction/increment field

646 The total number of operational AERONET sites has grown to over 300 in recent years. However,  
647 the network's global coverage is uneven with the majority of sites located over land where they are  
648 easily accessible. The available AERONET data is often not representative of major aerosol impact  
649 regions, and it does not optimally sample for the biases that remote sensing products may have (Shi et  
650 al., 2011b). In particular, open oceans have few AERONET sites.

651 In regions with sparse AERONET data coverage, aerosol sources and parameters, such as  
652 sedimentation and dry deposition for ocean regions, are tuned using satellite AOT assimilation  
653 correction/increment fields. The monthly means of the daily AOT corrections (i.e., the difference  
654 between the assimilation posterior and the model prior) are a good indicator of the model performance  
655 globally. The correction maps can be used to quickly identify geographic regions where the model  
656 succeeds or does poorly. A region in which the data assimilation consistently suppresses aerosol mass



657 could indicate a region with excessive aerosol emissions, or deficient removal, with the assumption that  
658 aerosol transport has much smaller uncertainty.

659 Since satellite products have uncertainties, especially over land, we rely on source corrections  
660 inferred from AERONET except where there are no representative sites close to the known source area  
661 (e.g., southern African biomass burning region). Over the ocean where AERONET has only a few sites  
662 globally, satellite data assimilation plays an irreplaceable role, not only because of the good spatial and  
663 temporal coverage of satellite AOT data, but also because of its much smaller uncertainty compared to  
664 the over-land AOT product (Hyer et al., 2011). Dust dry deposition velocity over water is tuned based on  
665 the AOT correction over the tropical Atlantic where African continent dust outflow is located, and is set  
666 to  $0.001 \text{ m s}^{-1}$ . To minimize the AOT correction over global ocean, especially high-latitude regions where  
667 surface wind is large, we also update the sea salt dry deposition velocity over water from a constant to a  
668 function of surface wind speed following Eq. (8). This effectively reduces the negative AOT correction  
669 over high-wind regions. This approach does not account for possible sources of error, including sea salt  
670 emission parameterization, biases in surface wind that drives emission and biases in boundary layer  
671 relative humidity that affects hygroscopic growth of the sea salt particles. In particular, our approach  
672 assumes that meteorological fields are correct, and implements correction solely to the uncertain  
673 parameters of aerosol sources and sinks.

674

### 675 **3.0 Reanalyzed Aerosol Optical Thickness**

676 In this section, we focus on evaluating the reanalysis AOT at 550 nm apportioned into fine and  
677 coarse mode contributions. The sum of the fine and coarse mode AOTs constitutes the total AOT. These  
678 are what we consider the key reanalysis output variables. Dust and sea salt are considered coarse-mode  
679 aerosols and the ABF and smoke aerosols are considered fine-mode aerosols, given the simple  
680 microphysics of the NAAPS model. Seasonally, the boreal winter/spring (December to next-May, ie.,

681 DJFMAM) and boreal summer/fall (June to November, ie., JJASON) time periods are investigated. When  
682 performing bi-seasonal long-term averaging, we use only data in June 2003-May 2013 time period, so  
683 that each individual month has an even weighting.

684

### 685 3.1 Global distribution of AOT and seasonal variability

686 | The bi-seasonally averaged total, fine, and coarse mode AOTs at ~~550nm~~550 nm for the 2003-2013  
687 time period are presented in Fig. 5. Results are shown for the reanalysis and a parallel model run using  
688 tuned source and sink parameters but without AOT data assimilation. The fused MODIS-MISR DA-quality  
689 AOT for the same time period are shown in Fig. 2 (right column) for comparison. The total AOTs for both  
690 the NAAPS runs with and without AOT data assimilation look very similar to the fused DA-quality  
691 MODIS-MISR AOT. Prominent fine mode features include pollution over East Asia and India, as well as  
692 biomass burning in South Africa, South America and the Maritime Continent in JJASON. Distinguishable  
693 coarse mode features include Saharan dust, Arabian and central Asian dust, and the circumpolar sea salt  
694 belt over the Southern Ocean. For DJFMAM, the total AOTs for both the NAAPS runs with and without  
695 AOT data assimilation also look very similar to the fused DA-quality MODIS-MISR AOT. As for the fine-  
696 mode AOT, in addition to the year-round pollution over East Asia and India, biomass burning in central  
697 Africa and Peninsular Southeast Asia shows up for the DJFMAM season. As for the coarse-mode AOT,  
698 dust over Sahara, Sahel, Arabian Peninsula and East Asia are clear and the circumpolar sea salt belt over  
699 the southern ocean is persistent. The seasonal global average total AOTs for over-ocean and over-land  
700 from the reanalysis are also similar to those of the fused DA-quality MODIS-MISR AOT. The NAAPS run  
701 without AOT assimilation has slightly higher global average total AOTs for over-ocean and over land,  
702 mainly attributed to higher fine mode AOT averages.

703           The similarity between the NAAPS runs with and without AOT data assimilation implies that the  
704 AOT correction by the data assimilation process is small and the whole model tuning process is effective.  
705 The resemblance between the reanalysis (NAAPS with AOT data assimilation) AOT and the fused MODIS-  
706 MISR AOT indicates that the data assimilation system works well in adjusting model fields to the closest  
707 observations. In this study, the model tuning process is considered equally as significant as the AOT data  
708 assimilation in influencing the final reanalysis. As the DA-quality satellite AOT data can reflect relatively  
709 small global coverage (Fig. 1, Fig. 2), areas not covered by the DA-quality satellite AOT would be highly  
710 impacted by the natural model (NAAPS without data assimilation). More details on the impact of tuning  
711 versus the DA on the model performance are provided in Appendix.

712           For this type of comparison (Fig. 5), which is done with all available model and satellite data, we  
713 should also expect some difference between the satellite retrievals and the reanalysis, resulting from  
714 contextual biases in satellite products such as clear sky biases (Zhang and Reid, 2009). Satellite retrievals  
715 for AOT mainly occur over clear sky, while the model depicts both clear and cloudy situations. Aerosol  
716 conditions can be very different between clear and cloudy sky, which is often associated with weather  
717 systems. For example, during the South America and Africa burning season (corresponding to JJASON),  
718 the southeast outflow regions from the southeast coast of the continents into the southern oceans are  
719 found to have lower seasonal average AOT for clear sky compared to cloudy/all sky, as smoke plumes  
720 are often transported along with the cloud system (Zhang and Reid, 2009). This clear sky bias is also  
721 discernable comparing MODIS AOT and the reanalysis AOT (Fig. 2 and Fig. 5).

722

### 723 3.2 Validation with AERONET

724           For validation purposes, we use the quality-assured AERONET Level-2 product. The reanalysis  
725 AOTs are compared with AERONET ~~6-hrly~~6-hourly total, fine and coarse mode AOTs at ~~550nm~~550 nm.

726 3.2.1 Global overview

727 Over the reanalysis period (2003-2013), the number of AERONET observations that can be  
728 paired with model data gradually increases with time (Fig. 6a). The daily volume of global ~~6-hrly~~6-hourly  
729 AERONET data has more than doubled in 2012 compared with 2003. The data count in 2013 decreases  
730 slightly due to the long processing time required for validating AERONET Level 2 data (instruments need  
731 to be removed from the field and recalibrated (Smirnov et al., 2000)). As there are more AERONET sites  
732 in the northern hemisphere than in the southern hemisphere and AERONET measurement only occurs  
733 during daytime, there are more AERONET observations during boreal summers than winters. Polar and  
734 high-latitude sites have few or no observations in winter, which raises a temporal sampling issue in  
735 validation for these regions. AERONET sampling also covaries with the seasonal AOT assimilation cycle,  
736 as high-latitude regions are less influenced by AOT assimilation during the wintertime.

737 Despite the uneven seasonal sampling, the ninety-day running average of the root mean square  
738 error (RMSE) of reanalysis AOTs is quite stable throughout the reanalysis time period (Fig. 6b), at around  
739 0.1 for both fine and coarse mode AOTs and 0.14 for the total AOTs. Daily average RMSE can  
740 occasionally exceed 0.4.

741 Figure 7 provides the comparison of the pair-wise ~~6-hrly~~6-hourly reanalysis AOT and AERONET  
742 AOT for all of the available global sites during the reanalysis time period. The normalized data density is  
743 shown in color. AOT data from AERONET and the reanalysis are binned at a resolution of 0.01 and  
744 density of each bin is colored relative to the maximum density in the sample. Also shown are the basic  
745 statistics of the comparison: the total number of stations and the ~~6-hrly~~6-hourly observations, bias, root-  
746 mean-square error (RMSE), square of the Pearson correlation coefficient ( $r^2$ ), and the linear regression  
747 parameters of the Theil-Sen method (Theil, 1950; Sen, 1968). The slope of the Theil-Sen linear  
748 regression is defined as the median of the slopes determined by all pairs of two-dimensional sample

749 points. It is a robust linear regression that is insensitive to outliers and more accurate than the least-  
750 squares regression for potentially skewed data. For reference, also shown is the linear least square  
751 regression line, which is more sensitive to outliers.

752 For both JJASON and DJFMAM, the global reanalysis fine-mode AOT has a small positive bias of  
753 slightly less than 0.01, while the coarse-mode AOT has a negative bias close to -0.02. The resulting bias  
754 for total AOT is -0.01. It is noteworthy that perhaps a portion of the AERONET coarse mode bias is due to  
755 cirrus contamination (Chew et al., 2011), which will be mitigated in the next major revision of AERONET  
756 data. The RMSE values for both fine and coarse mode ~~6-hrly~~6-hourly AOTs are  $\sim 0.1$ , except that the  
757 RMSE of the coarse AOT is a little higher (0.11) during DJFMAM and a little lower during JJASON (0.08).  
758 The seasonality of RMSE for coarse mode AOT is more apparent than that of the fine mode AOT, which  
759 is consistent with Fig. 6. RMSE for the total AOT is 0.14 for both seasons, consistent with Fig. 6 as well.  
760  $r^2$  is close to 0.65 for fine mode AOT and close to 0.61 for coarse mode AOT for both seasons.  $r^2$  for the  
761 total AOT is about 0.7, which is slightly better than the individual fine/coarse mode AOTs. The slope of  
762 the Theil-Sen regression lines is greater than 1 (around 1.3) for the fine mode AOT, less than 1 (around  
763 0.8) for the coarse mode AOT, and very close to 1 for the total AOT for both seasons. All of the above  
764 statistical numbers indicate that the fine mode AOT has a small high bias while the coarse mode AOT has  
765 a small low bias on average and globally. There is little seasonal difference in the mode statistics (fine,  
766 coarse and total modes) for the whole globe.

767 As monthly data is often used in climate studies, we also evaluate the reanalysis monthly  
768 averaged AOTs (Fig. 8). Monthly averages are obtained only when the total number of ~~6-hrly~~6-hourly  
769 AERONET data exceeds ten. For validation purposes, the monthly average reanalysis AOT is calculated  
770 based on the available ~~6-hrly~~6-hourly data that can be paired with AERONET data. With the high  
771 frequency signals (e.g., daily variability) smoothed out, the monthly average exhibits a better match with

772 AERONET data over all. For both seasons and all modal AOTs, the monthly averages in the scatter plots  
773 are more aligned with the 1:1 lines, RMSE is roughly 50% lower (0.07 for total AOT, 0.05 for fine and  
774 coarse mode AOTs), and  $r^2$  about 0.2 higher on average (with a maximum of 0.90 for the total AOT in  
775 DJFMAM and a minimum of 0.74 for the coarse AOT in JJASON). While absolute bias is unaffected by  
776 averaging, there appears a slope bias in linear regression results. Sites that may have a low background  
777 punctuated by severe events will appear in the regression differently from sites with a consistent but  
778 high background. This results in slope bias in regression of monthly averaged AOT values, demonstrating  
779 the dangers of applying monthly mean data to downstream calculations such as radiative forcing. Such  
780 calculations need to be conducted at the finest spatial and temporal scales achievable, with accounting  
781 for resolution effects.

782 Figure 9 shows the cumulative distribution function (CDF) of AOT errors compared with  
783 AERONET for total, fine and coarse AOTs, respectively, using ~~6-hrly~~6-hourly data. As a reassurance, the  
784 CDF of AOT errors compared with MODIS and MISR DA quality data is also shown. Because the seasonal  
785 differences for the global validation statistics are small, the two seasons are combined for the CDF  
786 analysis. As expected, the reanalysis total AOT is in good agreement with MODIS and MISR DA quality  
787 AOTs, though slightly less agreement with MISR than MODIS is found as the relative number of MISR  
788 data involved in AOT assimilation is much less. More than 95% of the reanalysis total AOT has an AOT  
789 error falling in the AOT error range of [-0.05, 0.05] compared with MODIS or MISR. The reanalysis AOT  
790 has larger errors with respect to AERONET. The crossing points of the CDF curves and the zero AOT error  
791 line (and the -0.1/+0.1 error lines) show that about 35% fine mode AOT has a low bias (4% with error  
792 less than -0.1) and the other 65% has a high bias (6% with error greater than 0.1) compared to AERONET.  
793 For coarse mode AOT, about 60% has a low bias (7% with error less than -0.1) and 40% has a high bias (2%  
794 with error greater than 0.1). For the total AOT, about 44% has a low bias (10% with error less than -0.1)

795 and 56% has a high bias (8% with error greater than 0.1). On average the fine AOT has a slight high bias  
796 and the coarse AOT has a slight low bias, which is consistent with the scatter plot result (Fig. 7).

### 797 3.2.2 Regional Evaluation

798 Figures 10, 11, and 12 show box-whisker plots of the pair-wise comparisons of regional  
799 reanalysis ~~6-hrly~~6-hourly modal AOT vs AERONET: percentiles marked in the plots are 95%, 90%, 75%,  
800 50%, 25%, 10% and 5%, for the regions defined in Fig. 4 for 2003-2013. Also shown are regional mean  
801 AOTs designated by a diamond for AERONET and “+” for the reanalysis. Detailed statistics associated  
802 with Fig. 10-12 (including separation into two seasons) are provided in the supplemental material.  
803 These include seasonal means and medians of the reanalysis and AERONET, along with reanalysis bias,  
804 RMSE,  $r^2$ , Theil-Sen linear regression parameters and number of valid data points for each region and  
805 the globe.

806 In general, the reanalysis follows the regional variation found in AERONET for fine-mode, coarse-  
807 mode and total AOTs. For the fine mode AOT, the reanalysis matches well with AERONET with respect  
808 to the regional means, medians, and variance. However, the results vary by region (Fig. 10). The  
809 regional means and medians are the same or slightly larger than those of AERONET for all regions,  
810 except East Asia and insular Southeast Asia, where the means are smaller than AERONET. The high AOT  
811 regions are the developing East Asia, Indian subcontinents, Peninsular and Insular Southeast Asia. These  
812 regions also have the highest RMSE values varying between 0.15 and 0.2, while RMSE values of other  
813 regions are all below 0.1. The low bias in mean fine mode AOT in East Asia and insular Southeast Asia is  
814 mostly due to the model’s inability to capture the magnitude of large fine aerosol events (e.g. extreme  
815 pollution and biomass burning events). The correlation coefficients ( $r^2$ ) of most regions fall between 0.5  
816 and 0.9. The best performing region is South America, whose  $r^2$  is greater than 0.8, indicating the  
817 reanalysis captures the temporal variation in fine mode aerosols, which are attributed mostly to biomass

818 burning smoke. Regions with worse  $r^2$  include West Continental United States (W. CONUS), North Africa,  
819 SW Asia and insular Southeast Asia, with  $r^2$  around 0.4-0.5.

820 The coarse mode AOT, overall, agrees less well with AERONET than the fine mode AOT with  
821 respect to the regional means, medians, variances and correlations (Fig. 11). Many regions have  
822 generally very low coarse AOT; RMSE for these regions will be low, but  $r^2$  will also be low due to the  
823 small dynamic range. The most prominent high coarse mode AOT regions are the dusty North Africa and  
824 Southwest Asia domains. The moderate coarse mode AOT regions are dust-influenced Indian  
825 subcontinent, East Asia and Central America. These regions have relatively large RMSE (between 0.1 and  
826 0.2), except central America (<0.1), compared to other regions (<0.1). Except for Southwest Asia, the  
827 oceanic region, North America boreal, W. CONUS and Australia, where the reanalysis mean coarse mode  
828 AOT is comparable to that of AERONET, other regions show mean low biases. The low bias, relative to  
829 the mean AOT, is generally small, except for Peninsular and insular Southeast Asia. The bias over these  
830 regions is attributed largely to the known thin cirrus contamination in AERONET L2 data (Chew et al.,  
831 2011; Huang et al., 2011). Thin cirrus cloud is a significant challenge for sun photometer aerosol optical  
832 ~~thickness~~ measurement, as it is easily miscategorized as coarse-mode aerosols by the instrument.  
833 The persistent occurrence of high thin cirrus cloud over these regions elevates the mean coarse mode  
834 AOT and thus the mean total AOT substantially. For example, at Singapore, a representative site for the  
835 insular Southeast Asia, 34% of AERONET L2 AOT data is found to be coincident with Micro-Pulse Lidar  
836 Network (MPLNET)-observed cirrus clouds (Chew et al., 2011). The estimated range of positive AOT bias  
837 in AERONET L2 data over Singapore, due to unscreened cloud presence, ranges from 0.03 to 0.06. Taking  
838 this estimated AOT bias of AERONET L2 data into account, the reanalysis coarse-mode AOT would be  
839 very close to reality. A similar situation exists for the peninsular Southeast Asia, based on the estimated  
840 cirrus cloud contamination in AERONET data at the regionally representative Pimai, Thailand site (Huang  
841 et al., 2011).



842 The correlation coefficients  $r^2$  of the coarse mode AOT are less than those of the fine mode AOT  
843 for most regions, except for north Africa, SW Asia, Europe-Mediterranean and India, which have strong  
844 dust influence. Insular and Peninsula SE Asia have the worst correlations as expected, mostly because of  
845 the cirrus cloud contamination in AERONET data. Other regions which have small AOT variations (e.g.  
846 dynamical data range less than 0.1) tend to have small  $r^2$  s, e.g., north American Boreal and W. CONUS.

847 The total AOT, which is the sum of the coarse-mode AOT and fine-mode AOT, has a validation  
848 feature that combines the validation properties of the two AOT modes (Fig. 12). The regional variation  
849 of total AOT follows that of AERONET well. The variance of the reanalysis for each region is smaller  
850 overall than that of AERONET, suggesting the difficulty in capturing extreme events with the model and  
851 assimilation system and a tendency to underestimate the magnitude of extreme events and  
852 overestimate in very clean conditions. A smaller AOT variance is known to be a typical model behavior  
853 among aerosol models (Kinne et al., 2006; Sessions et al., 2015) and is a persistent challenge to the  
854 aerosol modelling community. The reanalysis does not perform as well with respect to mean bias and  
855 RMSE over East Asia, Indian subcontinent, insular and peninsular Southeast Asia, where complicated  
856 aerosol environments often exist. For example, dust is often mixed with various kinds of pollutants over  
857 East Asia and the Indian subcontinent, which hinders satellite AOT retrievals and impacts model  
858 performance through AOT data assimilation. Over insular Southeast Asia, constant high cloud cover  
859 poses significant observability issues (Reid et al., 2013), reducing the availability of successful satellite  
860 retrievals of AOT, in addition to artificial high AOTs caused by cirrus contamination in AERONET data.  
861 This region also has a complicated fire regime that is systematically undersampled by the observations  
862 used to drive the smoke emissions in the model (Miettinen et al., 2013). The large discrepancies  
863 between the reanalysis and AERONET for coarse AOTs over insular and peninsular Southeast Asia affect  
864 the reanalysis means and medians for total AOTs, but to a lesser degree, since fine mode aerosols are  
865 the dominant aerosol type for the these regions. Most regions have  $r^2$  between 0.5 and 0.8. W. CONUS

866 has the smallest  $r^2$ , which is about 0.376, among all regions, reflecting the challenge for the model to  
867 simulate the small variance of the AOT there.

### 868 3.2.3 Site-by-site validation

869 Site-by-site validation of the NAAPS reanalysis was conducted relative to the International  
870 Cooperative for Aerosol Prediction (ICAP) Multi Model Ensemble (ICAP-MME, Sessions et al., 2015) as a  
871 baseline. Overall, ICAP-MME was shown to outperform any individual models with regard to RMSE in  
872 ~~550nm~~550 nm AOT forecast (Sessions et al., 2015). By ranking, the ICAP-MME was typically first or  
873 second against all models at individual sites using one-year worth of data. Since most of the ICAP  
874 models include AOT assimilation as well, the NAAPS reanalysis was compared to the ICAP-MME. The  
875 twenty-one AERONET sites used in the ICAP-MME study were agreed upon by the world's major center  
876 developers, as the most representative of each region. The same two seasonal periods (DJFMAM and  
877 JJASON of 2012) are used. In Fig. 4, these sites are marked with red squares. The ICAP-MME is run daily  
878 at 00 UTC for ~~6-hrly~~6-hourly forecasts out to 120 hr. The best available ICAP MME data (closest to  
879 analysis) for this comparison is the consensus mean of 6-hr forecast at 00 UTC; thus, the NAAPS  
880 reanalysis is at an advantage in this comparison due to the lagged AOT assimilation cycle in the ICAP-  
881 MME.

882 Table 2 shows the name of each site, its location and the prevailing aerosol type, along with all  
883 statistics relating to the total AOT at ~~550nm~~550 nm for the two seasons. The same statistics for fine and  
884 coarse mode AOTs are listed in Tables 3 and 4, respectively. The values of bias and RMSE are in bold,  
885 bold with underline, and italic, depending on whether the reanalysis performance is the same, better, or  
886 worse than the ICAP MME mean 6-hr forecast, respectively. Over a majority of the sites, the total AOT  
887 of the reanalysis is the same or better than the ICAP-MME with respect to bias and RMSE. The  
888 exceptions are the Beijing and Solar Village AERONET sites. Singapore is uncertain, as the low biases in

889 fine mode AOT contributes less than half of the total low bias, implying the dominant bias is the coarse  
890 mode AOT bias, which is affected by thin cloud contamination in AERONET data. Cases, where the  
891 reanalysis is the same or better than the ICAP-MME in bias and RMSE occur less for the coarse-mode  
892 AOT than for the total AOT. On the one hand, the total AOT is assimilated in the reanalysis while the  
893 coarse mode AOT is not. So, the total AOT is better constrained with satellite observations. On the  
894 other hand, the ICAP-MME consensus mean for dust/coarse mode AOT includes an additional  
895 independent aerosol model relative to the total AOT consensus (five vs. four models), which makes the  
896 dust AOT ensemble exhibit better performance among all the models compared with the total AOT  
897 ensemble performance (Sessions, et al., 2015).

898         The AOT seasonal difference is very clear for sites with outstanding seasonal aerosol features.  
899 For example, higher total and fine AOT values attributed to biomass burning are observed in JJASON  
900 over Alta Floresta, Rio Branco, and Singapore and in DJFMAM over Chiang Mai. Seasonal differences are  
901 also found over Ilorin with higher AOT in DJFMAM relative to JJASON, due to both dust and biomass  
902 burning activities. It is generally true that absolute bias and RMSE increase with increasing values of  
903 AOT, so a seasonal variation in bias and RMSE is also discernable for the sites with large seasonal AOT  
904 variations.  $r^2$  of the above sites in their biomass burning seasons are generally very good (above 0.8  
905 except for Singapore), indicating that the reanalysis captures the timing and variability of large smoke  
906 episodes quite well.

907         Overall, the sign of the bias and the order of magnitude of the bias and RMSE values for the  
908 selected sites are consistent with the regional evaluations in Fig. 10-12 (and the supplemental tables).  
909 For high AOT sites (e.g., Banizoumbou, Beijing, Chiang Mai, Gandhi College, Ilorin and Kanpur), the  
910 reanalysis generally has a low bias, as a result of the model and/or the data assimilation system being  
911 incapable of capturing the amplitude of high AOT events. An exception is Solar Village, though its

912 dominant aerosol species, which is dust/coarse mode aerosol, is also biased low in AOT during DJFMAM.  
913 Low bias in high AOT events is quite common among aerosols models (Kinne et al., 2006; Sessions et al.,  
914 2015). The discrepancy can arise solely as a function of spatial and temporal resolution: the average AOT  
915 for a grid cell in an aerosol plume will be systematically lower than the peak observed point AOT in that  
916 plume. However, shortcomings of aerosol sources or insufficient representation of near-source aerosol  
917 processes can also cause bias. Sometimes the discrepancy can be reduced by AOT assimilation, but the  
918 probability of a successful retrieval declines for higher AOT events, and this phenomenon is amplified by  
919 the application of AOT QA/QC procedures. The largest departure for both seasons in total AOT occurs  
920 over Beijing, where the coarse mode bias contributes a little more to the total bias in DJFMAM and the  
921 fine mode bias contributes a little more in JJASON. Among all sites, the maximum RMSE occurs over  
922 Beijing in both seasons for the total and the fine mode AOT and in DJFMAM for coarse mode AOT.  
923 JJASON RMSE is smaller for the reanalysis than for the ICAP-MME, implying that global models uniformly  
924 don't do well here. Correlation coefficient  $r^2$  of the coarse mode AOT at Beijing is also the worst for both  
925 seasons, while  $r^2$  values for the fine and total AOTs are reasonable (0.54 in DJFMAM and 0.76 in JJASON  
926 for total AOT, and a little better for fine AOT). The frequent mixture of pollution, dust, and clouds, along  
927 with varying surface properties also hinders satellite retrievals, not only reducing the number of  
928 successful retrievals but also contributing to large errors in retrieved AOT (e.g, Shi et al., 2011b; Zhang et  
929 al., 2014). Similar situations exist for Ilorin, where Sahelian biomass burning system is often mixed with  
930 dust episodes in DJFMAM, and for Gandhi College and Kanpur, the two Indian sites, in both seasons.

931 For moderate to low AOT sites, including Cart Site, Chapais, GSFC, Minsk, Moldova, Monterey  
932 and Palma de Mallorca, the reanalysis performs well, with the biases falling between -0.02 and 0.02,  
933 RMSE values less than half of their site mean AOTs for all modes (all less than 0.07), and  $r^2$  between  
934 0.42 and 0.85. Over Crozet Island, a remote oceanic site in the Southern Indian Ocean, the reanalysis has  
935 a relative large high bias (compared to its very low mean) likely due to overestimation of sea salt. On the

936 contrary, the fine mode AOT has a slight low bias, which may be an indication of insufficient DMS  
937 emission or too much removal.

938           Several sites are affected by similar aerosol sources at different distances, allowing us to  
939 examine transport phenomena using these sites. Banizoumbou, which is located deep in the Sahara, has  
940 the largest bias (negative) and RMSE, and the lowest  $r^2$  for the coarse and total AOT modes among all  
941 the African-dust-impacted sites. Capo Verde, located on an island off the west coast of North Africa, has  
942 high coarse mode AOT, but with much smaller bias and RMSE and high correlation ( $r^2$  is  $\sim 0.88$  for  
943 DJFMAM and  $\sim 0.77$  for JJASON for both total and coarse AOTs), benefiting from AOT assimilation.  
944 Farther downwind of north Africa and across the Atlantic Ocean, Ragged Point in Barbados, shows even  
945 smaller biases and RMSEs and very high correlation ( $r^2$  greater than 0.81 for total AOT in both season,  
946 and for coarse AOT in JJASON). Palma de Mallorca, which is a receptor site for Saharan dust transported  
947 across the Mediterranean Sea, has bias, RMSE and correlation similar to Ragged Point.

948           The performance of the reanalysis has a tendency to increase with the distance from the source  
949 region, especially over water. The main reasons for this are 1) aerosol models normally have larger  
950 uncertainties in aerosol sources than aerosol transports (Kinne et al., 2003), 2) there is limited satellite  
951 AOT data over the bright desert regions for the model to assimilate (Fig. 2), while there are a lot more  
952 opportunities for the model AOT to be corrected by assimilation along dust transport paths, and 3) the  
953 atmosphere acts to smooth out near-source variability that is often at finer scales than the effective  
954 resolution of the model. These effects can also be seen when comparing the reanalysis performance  
955 over Beijing and Baengyeong, an island site in South Korea downwind of Beijing, for both fine and  
956 coarse mode AOTs.

957 3.3 AOT trend

958           There is debate over the use of AOT reanalyses to document and understand climatic trends,  
959 similar to the debate associated with meteorological reanalysis. However, the decadal trends derived  
960 from the reanalysis are largely in line with other studies using stand-alone satellite products (Zhang and  
961 Reid, 2010; Hsu et al., 2012) for a similar time period. This helps to evaluate the reanalysis from another  
962 perspective. Figure 13 shows the trend of the deseasonalized total AOT over the whole reanalysis period  
963 (2003-2013), using the same calculation method as in Zhang and Reid (2010), where the significance of  
964 the trend analysis is estimated following the method of Weatherhead et al. (1998). Many areas show  
965 trends consistent with the satellite-only results of Zhang and Reid (2010) and Hsu et al. (2012): Indian  
966 Bay of Bengal, Arabian Peninsula and Arabian Sea, Bohai Sea in East Asia and the downwind region of  
967 South African biomass burning area, which have a positive trend, and the east coast of North America,  
968 Europe, central South America biomass burning area and Southern Indian Ocean, which have a negative  
969 trend. The reanalysis also exhibits a weak negative trend off the coast of dusty West Africa that is  
970 similar to other studies, though not statistically significant. The non-trend (zero trend) region with  
971 statistical significance in the south subtropical Pacific Ocean is also consistent with other studies.

972           An arguable trend appears in the Maritime Continent, where Zhang and Reid (2010) report a  
973 non-significant positive trend while Hsu et al. (2012) and our reanalysis here report a non-significant or  
974 significant negative trend based on slightly different study periods (Study periods are 2000-2010, 1998-  
975 2010, and 2003-2013 in Zhang and Reid, Hsu et al. and this paper, respectively). Because 1997-1998 was  
976 a strong El Nino period and 2010-2012 are La Nina years, corresponding to strong and weak fire  
977 activities in the Maritime Continent, respectively, trends for these different periods can be expected to  
978 differ systematically. Studies show that the climate and the associated fire/smoke activity in the  
979 Maritime Continent are controlled by ENSO on the inter-annual time scale (e.g., Reid et al., 2012; van  
980 der Werf et al., 2004). The Maritime Continent is anomalously dry during El Nino years and experiences  
981 more fire activity and thus smoke aerosols compared to La Nina years, and there is a good correlation

982 | between ENSO and AOT there (e.g., Hsu et al., 2012; Xian et al., 2013). The different AOT trends over the  
983 | maritime continents obtained with the use of slightly different time periods suggest the importance of  
984 | checking the possible controlling climate variability on aerosol trend analysis depending on the time  
985 | scales of interest. Similarly, the negative AOT trend in north Africa and off the coast of West Africa is  
986 | likely impacted by the Atlantic Multidecadal Oscillation (AMO), North Atlantic Oscillation (NAO) and  
987 | ENSO activities as Saharan dust is also shown to be correlated with these climate variabilities (Evan et al.,  
988 | 2006; Hsu et al., 2012; Wang et al., 2012).

989 |         This reanalysis uses non-trending source functions for sulfate, DMS, organic aerosol emissions  
990 | and dust erodibility. It is worth noting that even with static source functions and no volcanic source, the  
991 | data assimilation has successfully picked up the positive trend downwind of the Hawaiian Islands due to  
992 | the enhanced degassing activity of the Kilauea volcano since 2008 (e.g. Beirle et al., 2014). In a parallel  
993 | model run, where AOT data assimilation is turned off, trends disappear over the east coast of North  
994 | America and Europe or change sign over the Bay of Bengal while retaining their signs in most other  
995 | regions (not shown). This indicates that AOT trends over the eastern US, Europe and Bay of Bengal are  
996 | related to anthropogenic emission changes. Opposite to the trend shown in the DA run, West African  
997 | and the downwind subtropical Atlantic region show a strong positive trend in the natural run. There  
998 | could be many possible reasons, such as an artifact of stronger surface wind in the meteorological  
999 | model over the study period, or changes in vegetation which are not captured in the meteorological  
1000 | model or the dust source function.

1001 |         The positive trend over the Southern African biomass burning area and its downwind  
1002 | subtropical Atlantic region and the negative trend over central South America biomass burning region  
1003 | are by and large a result of increasing fire emissions over Southern Africa and decreasing fire emissions  
1004 | over South America exhibited in FLAMBE (not shown). The smoke emission trends in the above regions

1005 are consistent with the trends found with other satellite fire detection products for the same time  
1006 period (Giglio et al., 2013). Trends over other regions are most likely relevant to climate variability or  
1007 changes in climate, especially changes in meteorological variables that covary with aerosol processes.  
1008 For example, the aforementioned negative trend over the Maritime Continent is very likely closely  
1009 related to ENSO cycles. In another example, the decreasing dust trend in the North Africa dust outflow  
1010 region of the tropical Atlantic is shown to be caused mainly by a reduction in surface winds over dust  
1011 source regions rather than changes in land surface properties in modeling studies (Chin et al., 2014;  
1012 Ridley et al., 2014).

1013 The Arabian Peninsula experiences increasing AOT, which may result from the observed  
1014 decreasing precipitation for the similar time period (Almazroui et al., 2012). The negative AOT trend  
1015 over the Southern Indian Ocean is consistent with the trend analysis using MISR AOT data (Murphy,  
1016 2013). However, this trend in our analysis results solely from trends in the source and sink function,  
1017 because AOT is not assimilated in this region in our system. The decreasing trend in the southern Indian  
1018 Ocean AOT in the model is mainly caused by a decreasing trend in the surface winds in the  
1019 meteorological model, NOGAPS (not shown). Observational studies, however, have found that wind  
1020 speed over the southern oceans has increased in the past two decades (Young et al., 2011; Hande et al.,  
1021 2012). The question of why the surface wind in NOGAPS decreases and AOT decreases in the southern  
1022 oceans during the 2003-2013 time period requires additional investigation but beyond the scope of this  
1023 study.

1024 Figure 14 shows the monthly mean NAAPS reanalysis and AERONET L2 modal AOT at six AERONET  
1025 sites chosen for their relatively long-term record under different aerosol regimes: Alta Floresta in the  
1026 Amazon, dominated by biomass burning smoke during the burning season; Beijing in East Asia,  
1027 dominated by anthropogenic fine mode aerosols year round with mixed dust and pollutions in the spring



1028 time; Capo Verde off the west coast of North Africa, dominated by Sahara/Sahel dust, GSFC in east  
1029 CONUS, dominated by anthropogenic fine mode aerosols, Solar Village in the Arabian Peninsula,  
1030 dominated by dust, and Venice in Italy, dominated by pollution-related fine mode aerosols and  
1031 influenced by Saharan dust in spring time. Also shown are linear regression lines based on the total AOTs,  
1032 indicative of AOT trends. Annotations in each time series show bias, RMSE and  $r^2$  of the total AOT and  
1033 the dominant modal AOT, calculated with reanalysis monthly averages (unpaired). Statistics from a  
1034 paired comparison using reanalysis data sampled to match available AERONET data are shown in  
1035 parentheses.

1036 Overall, the reanalysis follows the seasonal and interannual variability in AERONET data for the  
1037 total AOT quite well, and to a lesser extent for the coarse and fine mode AOTs. The pairwise comparison  
1038 shows better correlation with AERONET than that calculated with all data, and, generally smaller  
1039 absolute bias and RMSE. The decreasing trends over Alta Floresta, GSFC and Venice, the increasing trend  
1040 over Beijing (slight) and Solar Village, and the insignificant trend over Capo Verde are consistent with the  
1041 regional trends shown in Fig. 13, and qualitatively agree with AERONET. Over GSFC, the reanalysis  
1042 captures the evident decrease in total and fine mode AOT since 2008. The June-July-August average AOT  
1043 drops about 0.14 (from 0.37 to 0.23) for the total AOT and 0.12 (from 0.29 to 0.17) for the fine mode  
1044 AOT comparing the years before and after 2008. It drops about 0.09 (from 0.31 to 0.22) for the total  
1045 AOT and 0.08 (from 0.27 to 0.19) for the fine mode AOT in the reanalysis, with a low bias in total AOT  
1046 and a minimal bias in fine mode AOT for the season.

#### 1047 **4 Summary and discussion**

1048 This paper describes a near 11-year global ~~550nm~~550 nm modal AOT reanalysis product developed  
1049 at the Naval Research Laboratory, with a spatial resolution of 1x1 degree and a temporal resolution of 6  
1050 hours. The reanalysis uses the Navy Aerosol Analysis and Prediction System (NAAPS) with regionally-

1051 tuned source functions at its core and assimilates quality-controlled Terra and Aqua Collection 5  
1052 Moderate Resolution Imaging Spectroradiometer (MODIS) and Multi-angle Imaging SpectroRadiometer  
1053 (MISR) AOT. Aerosol wet deposition in the tropics is constrained with satellite retrieved precipitation.  
1054 Dry deposition parameters over ocean are also adjusted by minimizing AOT corrections in AOT  
1055 assimilation. By validating the reanalysis fine and coarse mode AOTs and total AOT with Aerosol Robotic  
1056 Network (AERONET) Level-2 product, we report the following findings:

1057 *4.1 Global representation:* Compared with 6-hr-average AERONET data, global mean RSME values for  
1058 both fine and coarse mode AOTs are around 0.1, and the RMSE for the total AOT is  $\sim 0.14$ . AOT  
1059 RMSE decreases 50% when monthly averaging is applied. On a global average, coarse-mode AOT has  
1060 a slight negative bias (-0.02) which is partially compensated by a slight positive bias of the fine mode  
1061 AOT (0.01). In general, the fine mode AOT matches AERONET slightly better than the coarse mode  
1062 AOT, reflected in the bias, RMSE and correlation. These numbers vary among different regions  
1063 presumably because of regionally specific aerosol features.

1064 Since total AOT is being assimilated, the total AOT has a smaller uncertainty relative to the  
1065 coarse and fine mode AOT. Currently, there is no way to validate speciated AOTs if two or more  
1066 aerosol species are present in the same size mode. We would expect the relative uncertainty of the  
1067 speciated AOTs to be larger than the modal AOTs. The data quality of satellite-retrieved AOT is  
1068 generally better over water than over land because of the relatively simple surface optical  
1069 properties of water (e.g., Levy et al., 2005, Remer et al., 2005). Under the same AOT data  
1070 assimilation frequency (or same amount of data to be assimilated), the reanalysis performs  
1071 relatively better over oceanic and coastal regions/sites than land regions/sites.

1072 *4.2 Regional representation:* The reanalysis captures the regional and seasonal AOT variations skillfully.  
1073 The range of the regional reanalysis AOT values are generally smaller than those of AERONET (i.e.,  
1074 high bias for small AOTs and low bias for high AOTs), which is commonly seen among aerosol models,

1075 | especially with coarse spatial and temporal resolution (e.g., Kinne et al., 2006; Sessions et al., 2015).  
1076 | Challenging regions for the reanalysis are East Asia, Indian subcontinent and Sahel, where there are  
1077 | often mixed fine and coarse mode aerosols. The reanalysis generally performs better in the long-  
1078 | range transport regions than the source regions. For example, the reanalysis AOT of the Caribbean  
1079 | islands sites, which are the receptor sites of African dust, matches AERONET observations better  
1080 | than the land sites within the African continent. A field campaign analysis of remotely transported  
1081 | smoke aerosols from Borneo and Sumatra islands found good agreement between the reanalysis  
1082 | AOT and the smoke concentrations therein and in-situ measurements taken in the open ocean west  
1083 | of the Philippines (Reid et al., 2014).

1084 | *4.3 Trends:* The trends calculated from the reanalysis are similar to other studies using standalone  
1085 | satellite products (Zhang and Reid, 2010; Hsu et al., 2012) in both aerosol transport regions and  
1086 | source regions. Over regionally representative sites, the reanalysis trend in modal AOT also agrees  
1087 | qualitatively well with the trend in AERONET data. This provides a reassurance of the quality of the  
1088 | reanalysis product. It is also worth noting that without trending source functions for sulfate and  
1089 | organic aerosols precursors, the data assimilation system has successfully reproduced regional AOT  
1090 | trends that are related to emission changes in the past decade. For example, a positive trend over  
1091 | India is attributed to emission growth. Signals of other low-frequency climate variability are also  
1092 | discernable in the reanalysis AOT. For example, using an earlier version of the NAAPS AOT analysis,  
1093 | the modulation effect of the Madden-Julian Oscillation on smoke AOT over the Maritime Continent  
1094 | is found (Reid et al., 2012).

1095 | *4.4 Role of AOT data assimilation:* Overall, the data assimilation system is very effective in correcting  
1096 | the modeled AOT and bringing it as close as possible to the satellite observations, and spreading the  
1097 | information to the neighboring grid cells through a correlation length scale. In the time steps  
1098 | following assimilation, the information is further propagated downstream. The data assimilation

1099 system plays an indispensable role in picking up AOT trends in the regions affected by emission  
1100 changes that are not represented in the model. However, the data assimilation system, associated  
1101 with the assimilatable data, also has limitations. Satellite AOT retrievals characterize the optical  
1102 properties of a column, and it does not carry any information about aerosol vertical profiles or  
1103 speciation. So the total AOT is constrained through AOT data assimilation. The relative vertical  
1104 profile in 3-D extinction and speciation of the aerosols are uniformly varied to match the posterior  
1105 AOT. The geographical coverage of the MODIS+MISR data to be assimilated can cover only up to  
1106 about a quarter of the Earth in one data assimilation cycle (Fig. 1). AOT of one area can be updated  
1107 by the data assimilation system only once per day on average (at most twice per day) and only  
1108 during the local daytime. This affects the aerosol diurnal cycle in the reanalysis, as all the nighttime  
1109 AOT are purely driven by the natural model while daytime AOT can be controlled by the data  
1110 assimilation system. Repetitively adding or shedding aerosol mass and thus AOT in one area through  
1111 data assimilation can make the AOT evolution unphysical. Because AERONET measurements occur  
1112 during the local daytime, the validation results here may not represent the reanalysis skill for other  
1113 times of day.

1114 *4.5 Data consistency in time:* Even though the data assimilation system has the capability of capturing  
1115 the trend observed in stand-alone satellite or AERONET AOT analyses, the inconsistency in the  
1116 meteorological analysis of Navy Operational Global Atmospheric Prediction System (NOGAPS) in the  
1117 past decade poses a big challenge in the development of a long term global AOT reanalysis product.  
1118 NOGAPS experienced several upgrades in the reanalysis period, including improved land surface  
1119 parameterization, which impacts dust production trends.

1120 A meteorological reanalysis is intended to provide a more consistent atmospheric state for  
1121 aerosol simulations. But meteorological reanalyses have a data consistency issue as well, because  
1122 observations being assimilated change significantly with time (e.g., Dee et al., 2011). For example,

1123 with the ever-increasing satellite observations of the past two decades, more and more satellite  
1124 data are being assimilated for one or more meteorological variables. With the demise or periodic  
1125 malfunction of some satellite instruments, some data became unavailable. This impacts the final  
1126 meteorological reanalysis, and consequently the AOT reanalysis. The NOAA Climate Prediction  
1127 Center MORPHing (CMORPH) precipitation data, which is used to replace NOGAPS precipitation in  
1128 the Tropics, is only available after December 2002. Its usage can impact regional AOT significantly in  
1129 a natural model run (Xian et al., 2009). For areas not covered by the CMORPH product, any model  
1130 precipitation performance change in time can be a potential issue for AOT trend analysis.

#### 1131 *4.6 Recommendations for application*

- 1132 a) It is ideal for quick and consistent identification of large aerosol events globally or regionally. It  
1133 can serve as a reference and provide the general background aerosol information without  
1134 temporal or spatial discontinuity for field campaign analysis.
- 1135 b) The reanalysis AOT can be used to provide global and regional AOT climatologies for climate and  
1136 applied science applications.
- 1137 c) The reanalysis AOT can be used in different scale analysis, from daily to inter-annual. The diurnal  
1138 AOT analysis should be performed with caution considering the possible artifact feature  
1139 introduced by the AOT assimilation cycle.

1140 Our future direction for the NAAPS aerosol reanalysis will be focused on 3-D extinction and mass  
1141 concentration of single aerosol species, with special emphasis on the vertical dimension. The ability of  
1142 NAAPS assimilating the Cloud-Aerosol Lidar with Orthogonal Polarization (CALIOP) lidar backscatter  
1143 coefficient data (Campbell et al., 2010; Zhang et al., 2011, 2014) will aid in this effort.

1144

1145 **Code and data availability:**

1146 The NAAPS model code is a property of the U.S. Naval Research Laboratory and is not available to the  
1147 public. However, the NAAPS reanalysis data is available at [http://usgodae.org/cgi-](http://usgodae.org/cgi-bin/datalist.pl?dset=nrl_naaps_reanalysis&summary=Go)  
1148 [bin/datalist.pl?dset=nrl\\_naaps\\_reanalysis&summary=Go](http://usgodae.org/cgi-bin/datalist.pl?dset=nrl_naaps_reanalysis&summary=Go) . The data on this server are updated as model  
1149 improvements are made and reruns are completed.  
1150

#### 1151 **Acknowledgement:**

1152 The development of the NAAPS reanalysis was an outcome of the needs of multiple projects, and largely  
1153 supported by the Office of Naval Research Code 322 and the NASA Interdisciplinary Science Program.  
1154 Additional support was provided by the NRL Base Program and the Office of Naval Research 35. The  
1155 development team is grateful to the effort of the operational NASA-MODIS and MISR aerosol teams for  
1156 the development and implementation of their level two products. We are likewise grateful to the NASA  
1157 land team for the development of their fire products. The NASA Aerosol Robotic Network (AERONET)  
1158 data is key to verifying models such as the NAAPS reanalysis and the use of this federated network's  
1159 data is gratefully acknowledged.

#### 1160 **References:**

- Ahmadov R., McKeen S.A., Robinson A.L., Bahreini R., Middlebrook A., deGouw J., Meagher J., Hsie E.-Y., Edgerton E., Shaw S., Trainer M.: A volatility basis set model for summertime secondary organic aerosols over the eastern U.S. in 2006. *J. Geophys. Res.*, 117, D06301, doi:10.1029/2011JD016831, 2012.
- Almazroui, M., Nazrul Islam, M., Athar, H., Jones, P. D. and Rahman, M. A.: Recent climate change in the Arabian Peninsula: annual rainfall and temperature analysis of Saudi Arabia for 1978–2009. *Int. J. Climatol.*, 32, 953–966, 2012.
- Antoine, D., and Nobileau, D.: Recent increase of Saharan dust transport over the Mediterranean Sea, as revealed from ocean color satellite (SeaWiFS) observations, *J. Geophys. Res.*, 111, D12214, doi:10.1029/2005JD006795, 2006.
- Bathe, K.J. : *Finite Element Procedures*. Cambridge, MA: Klaus-Jürgen Bathe. ISBN 097900490X, 2006.
- Beirle, S., Hörmann, C., Penning de Vries, M., Dörner, S., Kern, C., and Wagner, T.: Estimating the volcanic emission rate and atmospheric lifetime of SO<sub>2</sub> from space: a case study for Kīlauea volcano, Hawai`i, *Atmos. Chem. Phys.*, 14, 8309–8322, 2014.
- Benedetti, A., Morcrette, J.-J., Boucher, O., Dethof, A., Engelen, R. J., Fisher, M., Flentje, H., Huneeus, N., Jones, L., Kaiser, J. W., Kinne, S., Mangold, A., Razinger, M., Simmons, A. J., and Suttie, M.: Aerosol analysis and recast in the European centre for Medium-Range Weather Forecasts Integrated Forecast System: 2. Data assimilation, *J. Geophys. Res.*, 114, D13205, doi:10.1029/2008JD011115, 2009.
- Benkovitz, C. M., T. Scholtz, L. Pacyna, L. Tarrson, J. Dignon, E. Voldner, P. A. Spiro, and T. E. Graedel : Global gridded inventories of anthropogenic emissions of sulphur and nitrogen. *J. Geophys. Res.*, 101, 29239–29253, 1996.
- Bond, T. C., D. G. Streets, K. F. Yarber, S. M. Nelson, J.-H. Woo, and Z. Klimont, A technology-based global inventory of black and organic carbon emissions from combustion, *J. Geophys. Res.*, 109, D14203, doi:10.1029/2003JD003697, 2004.
- Bond, T. C., et al.: Bounding the role of black carbon in the climate system: A scientific assessment, *J. Geophys. Res. Atmos.*, 118, 5380–5552, 2013.

- Buchard, V., da Silva, A. M., Colarco, P. R., Darmenov, A., Randles, C. A., Govindaraju, R., Torres, O., Campbell, J., and Spurr, R.: Using the OMI aerosol index and absorption aerosol optical depth to evaluate the NASA MERRA Aerosol Reanalysis, *Atmos. Chem. Phys.*, 15, 5743-5760, 2015.
- Campbell, J. R., J. S. Reid, D. L. Westphal, J. Zhang, E. J. Hyer, and E. J. Welton: CALIOP aerosol subset processing for global aerosol transport model data assimilation, *J of Sel. Topics in Appl. Earth Obs. and Rem. Sens.*, 3, 203-214, 2010.
- Campbell, J. R., Reid, J. S., Westphal, D. L., Zhang, J., Tackett, L., Chew B. N., Welton, E. J., Shimizu, A., Sugimoto, N., Aoki, K., Winker, D. M., Characterizing the vertical profile of aerosol particle extinction and linear depolarization over Southeast Asia and the Maritime Continent: The 2007–2009 view from CALIOP, *Atmos. Res.*, 122, 520-543, 2013.
- Chew, B. N., J. R. Campbell, J. S. Reid, D. M. Giles, E. J. Welton, S. V. Salinas and S. C. Liew: Tropical cirrus cloud contamination in sun photometer data, *Atmos. Environ.*, 45, 6724-6731, 2011.
- Chin, M, Diehl T, Tan Q, Prospero J, Kahn R, Remer L, Yu H, Sayer A, Bian H, Geogdzhayev I, Holben B, Howell S, Huebert B, Hsu N, Kim D, Kucsera T, Levy R, Mishchenko M, Pan X, Quinn P, Schuster G, Streets D, Strode S, Torres O, Zhao X.: Multi-decadal aerosol variations from 1980 to 2009: a perspective from observations and a global model. *Atmos. Chem. Phys.* 14, 3657-3690, 2014.
- Christensen, J. H. :The Danish eulerian hemispheric model—A three dimensional air pollution model used for the Arctic, *Atmos. Environ.*, 31, 4169-4191, 1997.
- Colarco, P., A. da Silva, M. Chin, and T. Diehl: Online simulations of global aerosol distributions in the NASA GEOS-4 model and comparisons to satellite and ground-based aerosol optical depth, *J. Geophys. Res.*, 115, D14207, doi:10.1029/2009JD012820, 2010.
- Collins, W. D., P. J. Rasch, B. E. Eaton, B. V. Khatatov, J.-F. Lamarque, and C. S. Zender: Simulating aerosols using a chemical transport model with assimilation of satellite aerosol retrievals: Methodology for INDOEX, *J. Geophys. Res.*, 106, 7313–7336, 2001.
- Dai, A.: Precipitation characteristics in eighteen coupled climate models, *J. Climate*, 19, 4605-4630, 2006.
- Daley, R. and Barker, E.: NAVDAS: Formulation and diagnostics, *Mon. Weather Rev.*, 129, 869-883, 2001.
- Dee, D. P., Uppala, S. M., Simmons, A. J., Berrisford, P., Poli, P., Kobayashi, S., Andrae, U., Balmaseda, M. A., Balsamo, G., Bauer, P., Bechtold, P., Beljaars, A. C. M., van de Berg, L., Bidlot, J., Bormann, N., Delsol, C., Dragani, R., Fuentes, M., Geer, A. J., Haimberger, L., Healy, S. B., Hersbach, H., Hólm, E. V., Isaksen, I., Kållberg, P., Köhler, M., Matricardi, M., McNally, A. P., Monge-Sanz, B. M., Morcrette, J.-J., Park, B.-K., Peubey, C., de Rosnay, P., Tavolato, C., Thépaut, J.-N. and Vitart, F. : The ERA-Interim reanalysis: configuration and performance of the data assimilation system. *Q.J.R. Meteorol. Soc.*, 137, 553–597, 2011.
- Diehl, T., Heil, A., Chin, M., Pan, X., Streets, D., Schultz, M., and Kinne, S.: Anthropogenic, biomass burning, and volcanic emissions of black carbon, organic carbon, and SO<sub>2</sub> from 1980 to 2010 for hindcast model experiments, *Atmos. Chem. Phys. Disc.* 12 : 24895-24954, 2012.
- Donahue, N. M., A. L. Robinson, C. O. Stanier, and S. N. Pandis: Coupled partitioning, dilution, and chemical aging of semivolatile organics. *Environ. Sci. Technol.* 40, 2635 – 2643, 2006.
- Dubovik, O., Holben, B., Eck, T. F., Smirnov, A., Kaufman, Y. J., King, M. D., Tanré, D. and Slutsker, I.: Variability of Absorption and Optical Properties of Key Aerosol Types Observed in Worldwide Locations. *J. Atmos. Sci.*, 59, 590–608, 2002.
- Evan, A. T., A. K. Heidinger, and P. Knippertz: Analysis of winter dust activity off the coast of West Africa using a new 24-year over-water advanced very high resolution radiometer satellite dust climatology, *J. Geophys. Res.*, 111, D12210, doi:10.1029/2005JD006336, 2006.
- Fromm, M. D., and R. Servranckx: Transport of forest fire smoke above the tropopause by supercell

- convection, *Geophys. Res. Lett.*, 30(10), 1542, doi:10.1029/2002GL016820, 2003.
- Giglio, L., J. T. Randerson, and G. R. van der Werf: Analysis of daily, monthly, and annual burned area using the fourth-generation global fire emissions database (GFED4), *J. Geophys. Res. Biogeosci.*, 118, doi:10.1002/jgrg.20042, 2013.
- Ginoux, Paul, M Chin, I Tegen, J M Prospero, B Holben, O Dubovik, and Shian-Jiann Lin: Sources and distributions of dust aerosols simulated with the GOCART model. *J. Geophys. Res.*, 106(D17), 20255-20273, 2001.
- Gordon, H. R. : Atmospheric correction of ocean color imagery in the Earth Observing System era, *J. Geophys. Res.*, 102(D14), 17081–17106, 1997.
- Granier, Claire et al., Evolution of anthropogenic and biomass burning emissions of air pollutants at global and regional scales during the 1980–2010 period, *Climate Change* 109 (1-2): 163-190, 2011.
- Hande, L. B., S. T. Siems, and M. J. Manton: Observed Trends in Wind Speed over the Southern Ocean, *Geophys. Res. Lett.*, 39, L11802, doi:10.1029/2012GL051734, 2012.
- Hanel, Hanel, G.: The properties of atmospheric aerosol particles as functions of relative humidity at thermodynamic equilibrium with surrounding moist air, *Geophys.*, 19, 73-188., 1976.
- Heald, C. L., D. J. Jacob, P. I. Palmer, M. J. Evans, G. W. Sachse, H. B. Singh, and D. R. Blake, Biomass burning emission inventory with daily resolution: Application to aircraft observations of Asian outflow, *J. Geophys. Res.*, 108(D21), 8811, doi:10.1029/2002JD003082, 2003.
- Hegg, D. A., D. S. Covert, K. Crahan, and H. H. Jonsson, The dependence of aerosol light-scattering on RH over the Pacific Ocean, *Geophys. Res. Lett.*, 29(8), doi:10.1029/2001GL014495, 2002.
- Hertel, O., Christensen, J., Runge, E., Asman, W. A. H., Berkowicz, R., Hovmand, M. and Hov, O.: Development and testing of a new variable scale air pollution model-ACDEP. *Atmos. Env.*, 29, 1267-1290, 1995.
- Hess, M., P. Koepke, P., and Schult, I.: Optical Properties of Aerosols and Clouds: The Software Package OPAC. *Bull. Amer. Meteor. Soc.*, 79, 831–844, 1998.
- Hoffmann, M. R. and Calvert, J. G.: Chemical Transformation Modules for Eulerian Acid Deposition Models: Volume II, the Aqueous-phase Chemistry, U.S. Environmental Protection Agency, Research Triangle Park, NC. 1985.
- Hogan, T. F. and L. Brody: Sensitivity Studies of the Navy's Global Forecast Model Parameterizations and Evaluation of Improvements to NOGAPS. *Mon. Wea. Rev.*, 121, 2373-2395, 1993.
- Hogan, T. F., Liu, M., Ridout, J. S., Peng, M. S., Whitcomb, T. R., Ruston, B. C., Reynolds, C. A., Eckermann S. D., Moskaitis, J. R., Baker, N. L., McCormack, J. P., Viner, K. C., McLay, J. G., Flatau, M. K., Xu, L., Chen, C., and Chang, S. W.,: The Navy Global Environmental Model. *Oceanography, Special Issue on Navy Operational Models*, 27, No. 3. 2014.
- Hogan, T.F. and T.E. Rosmond: The description of the Navy Operational Global Atmospheric Prediction System's spectral forecast model. *Mon. Wea. Rev.*, 119, 1786-1815, 1991.
- Holben, B. N., Eck, T. F., Slutsker, I., Tanre, D., Buis, J. P., Setzer, A., Vermote, E., Reagan, J. A., Kaufman, Y. J., Nakajima, T., Lavenu, F., Jankowiak, I., and Smirnov, A.: AERONET - A federated instrument network and data archive for aerosol characterization, *Remote Sens. Environ.*, 66, 1-16, 1998.
- Holben, B. N., Tanré, D., Smirnov, A., Eck, T. F., Slutsker, I., Abuhassan, N., Newcomb, W. W., Schafer, J. S., Chatenet, B., Lavenu, F., Kaufman, Y. J., Castle, J. V., Setzer, A., Markham, B., Clark, D., Frouin, R., Halthore, R., Karneli, A., O'Neill, N. T., Pietras, C., Pinker, R. T., Voss, K., and Zibordi, G.: An emerging ground-based aerosol climatology: Aerosol optical depth from AERONET, *J. Geophys. Res.-Atmos.*, 106, 12067-12097, 2001.
- Houweling, S., W. Hartmann, I. Aben, H. Schrijver, J. Skidmore, G.-J. Roelofs, and F.-M. Breon: Evidence of systematic errors in SCIAMACHY-observed CO<sub>2</sub> due to aerosols, *Atmos. Chem. Phys.*, 5, 3003–3013, 2005.
- Hsu, N. C., Gautam R, Sayer A, Bettenhausen C, Li C, Jeong M, Tsay S, Holben B. Global and regional



- trends of aerosol optical depth over land and ocean using SeaWiFS measurements from 1997 to 2010. *Atmos. Chem. Phys.* 12, 8037-8053, 2012.
- Hsu, N. C., Tsay, S.-C., King, M. D., and Herman, J. R.: Aerosol properties over bright-reflecting source regions, *IEEE T. Geosci. Remote Sens.*, 42, 557–569, 2004.
- Huang, J., N. C. Hsu, S.-C. Tsay, M.-J. Jeong, B. N. Holben, T. A. Berkoff, and E. J. Welton: Susceptibility of aerosol optical thickness retrievals to thin cirrus contamination during the BASE-ASIA campaign, *J. Geophys. Res.*, 116, D08214, doi:10.1029/2010JD014910, 2011.
- Hyer, E. J., Reid, J. S., Prins, E. M., Hoffman, J. P., Schmidt, C. C., Miettinen, J. I., Giglio L., Patterns of fire activity over Indonesia and Malaysia from polar and geostationary satellite observations, *Atmos. Res.*, 122, 504-519, 2013
- Hyer, E. J., Reid, J. S., and Zhang, J.: An over-land aerosol optical depth data set for data assimilation by filtering, correction, and aggregation of MODIS Collection 5 optical depth retrievals, *Atmos. Meas. Tech.*, 4, 379–408, 2011.
- Inness, A., Baier, F., Benedetti, A., Bouarar, I., Chabrilat, S., Clark, H., Clerbaux, C., Coheur, P., Engelen, R. J., Errera, Q., Flemming, J., George, M., Granier, C., Hadji-Lazarou, J., Huijnen, V., Hurtmans, D., Jones, L., Kaiser, J. W., Kapsomenakis, J., Lefever, K., Leitão, J., Razinger, M., Richter, A., Schultz, M. G., Simmons, A. J., Suttie, M., Stein, O., Thépaut, J.-N., Thouret, V., Vrekoussis, M., Zerefos, C., and the MACC team: The MACC reanalysis: an 8 yr data set of atmospheric composition, *Atmos. Chem. Phys.*, 13, 4073-4109, 2013.
- IPCC: Climate Change 2007: The Physical Science Basis. Contribution of Working Group I to the Fourth Assessment Report of the Intergovernmental Panel on Climate Change [Solomon, S., D. Qin, M. Manning, Z. Chen, M. Marquis, K.B. Averyt, M. Tignor and H.L. Miller (eds.)]. Cambridge University Press, Cambridge, United Kingdom and New York, NY, USA, 2007.
- IPCC: Climate Change 2013: The Physical Science Basis. Contribution of Working Group I to the Fifth Assessment Report of the Intergovernmental Panel on Climate Change [Stocker, T.F., D. Qin, G.-K. Plattner, M. Tignor, S.K. Allen, J. Boschung, A. Nauels, Y. Xia, V. Bex and P.M. Midgley (eds.)]. Cambridge University Press, Cambridge, United Kingdom and New York, NY, USA, 2013.
- Iversen, T.: Numerical modeling of the long range atmospheric transport of sulphur dioxide and particulate sulphate to the arctic, *Atmos. Environ.*, 23, 2571–2595, 1989.
- Janowiak, J.E., Kousky, V.E., Joyce, R.J.: Diurnal cycle of precipitation determined from the CMORPH high spatial and temporal resolution global precipitation analyses. *J. Geophys. Res.* 110, D23105, 2005.
- Jeong, J. I., Park, R., Woo, J.-H., Han Y.-J. and Yi, S.-M.: Source contributions to carbonaceous aerosol concentrations in Korea. *Atmos. Environ.*, 45, 1116-1125, 2011.
- Jimenez, J. L. et al.: Evolution of organic aerosols in the atmosphere. *Science*, 326, 1525-1529, 2009.
- Joyce, R.J., Janowiak, J.E., Arkin, P.A., Xie, P.: CMORPH: a method that produces global precipitation estimates from passivemicrowave and infrared data at high spatial and temporal resolution. *J. Hydromet.* 5, 487–503, 2004.
- Kahn, R. A., B. J. Gaitley, M. J. Garay, D. J. Diner, T. F. Eck, A. Smirnov, and B. N. Holben: Multiangle Imaging Spectroradiometer global aerosol product assessment by comparison with the Aerosol Robotic Network, *J. Geophys. Res.*, 115, D23209, doi:10.1029/2010JD014601, 2010.
- Kahn, R. A., Nelson, D. L., Garay, M., Levy, R. C., Bull, M. A., Diner, D. J., Martonchik, J. V., Paradise, S. R., and Hansen, E. G., and Remer, L. A.: MISR Aerosol product attributes, and statistical comparisons with MODIS. *IEEE Trans. Geosci. Remt. Sens*, 47, 4095–4114, 2009.
- Kahn, R. A., Y. Chen, D. L. Nelson, F.-Y. Leung, Q. Li, D. J. Diner, and J. A. Logan: Wildfire smoke injection heights: Two perspectives from space, *Geophys. Res. Lett.*, 35, L04809, doi:10.1029/2007GL032165. 2008.
- Kaku, K. C., J. S. Reid, N. T. O'Neill, P. K. Quinn, D. J. Coffman, and T. F. Eck: Verification and application

- of the extended spectral deconvolution algorithm (SDA+) methodology to estimate aerosol fine and coarse mode extinction coefficients in the marine boundary layer, *Atmos. Meas. Tech.*, 7, 3399-3412, 2014.
- Kalnay, E., M. Kanamitsu, R. Kistler, W. Collins, D. Deaven, L. Gandin, M. Iredell, S. Saha, G. White, J. Woollen, Y. Zhu, A. Leetmaa, R. Reynolds, M. Chelliah, W. Ebisuzaki, W. Higgins, J. Janowiak, K. C. Mo, C. Ropelewski, J. Wang, R. Jenne, D. Joseph: The NCEP/NCAR 40-year reanalysis project, *Bull. Amer. Meteor. Soc.*, 77, 437-470, 1996.
- Kappos, A. D., Brickmann, P., Elkmann, T., et al.: Health effects of particles in the ambient air, *Int. J. of Hygiene and Environ. Health*, 207, 399-407, 2004.
- Kinne, S., et al.: An AeroCom initial assessment -- optical properties in aerosol component modules of global models. *Atmos. Chem. Phys.* 6, 1815-1834, 2006.
- Kinne, S., et al., Monthly averages of aerosol properties: A global comparison among models, satellite data, and AERONET ground data, *J. Geophys. Res.*, 108(D20), 4634, doi:10.1029/2001JD001253, 2003.
- Laden, F., Neas, L. M., Dockery, D. W., and Schwartz, J.: Association of fine particulate matter from different sources with daily mortality in six US cities, *Environ. Health Perspectives*, 108, 941-947, 2000.
- Lana, A., et al.: An updated climatology of surface dimethylsulfide concentrations and emission fluxes in the global ocean, *Global Biogeochem. Cycles*, 25, GB1004, doi:10.1029/2010GB003850. 2011.
- Levy, R. C., Remer, L. A., Kleidman, R. G., Mattoo, S., Ichoku, C., Kahn, R., and Eck, T. F.: Global evaluation of the Collection 5 MODIS dark-target aerosol products over land, *Atmos. Chem. Phys.*, 10, 10399-10420, 2010.
- Levy, R. C., Remer, L. A., Mattoo, S., Vermote, EF, Kaufman, Y. J.: Second-generation operational algorithm: Retrieval of aerosol properties over land from inversion of Moderate Resolution Imaging Spectroradiometer spectral reflectance. *J. Geophys. Res.-Atmos.* 112, D13211, doi:10.1029/2006JD007811, 2007.
- Levy, R. C., et al.: Evaluation of the MODIS aerosol retrievals over ocean and land during CLAMS, *J. Atmos. Sci.*, 62(4), 974-992, 2005.
- Li-Jones X, H. B. Maring, J. M. Prospero: Effect of relative humidity on light scattering by mineral dust aerosol as measured in the marine boundary layer over the tropical Atlantic Ocean, *J. Geophys. Res.* 103, 31113-31121, 1998.
- Martonchik, J. V., R. A. Kahn, and D. J. Diner, "Retrieval of aerosol properties over land using MISR observations," in *Satellite Aerosol Remote Sensing Over Land*, A. Kokhanovsky, Ed. Berlin, Germany: Springer-Verlag, 2009.
- May, D. A., Stowe, L. L., Hawkins, J. D., McClain, E. P.; A correction for Saharan dust effects on satellite sea-surface temperature-measurements, *J. Geophys. Res.*, 97, 3611-3619, 1992.
- Miettinen, J., E. Hyer, A. S. Chia, L. K. Kwoh, and S. C. Liew: Detection of vegetation fires and burnt areas by remote sensing in insular Southeast Asian conditions: current status of knowledge and future challenges, *Int. J. Remote Sens.*, 34(12), 4344-4366, 2013.
- Miller, R.L., R.V. Cakmur, J.P. Perlwitz, I.V. Geogdzhayev, P. Ginoux, K.E. Kohfeld, D. Koch, C. Prigent, R. Ruedy, G.A. Schmidt, and I. Tegen: Mineral dust aerosols in the NASA Goddard Institute for Space Sciences ModelE atmospheric general circulation model. *J. Geophys. Res.*, 111, D06208, doi:10.1029/2005JD005796, 2006.
- Ming, Y, Russell L. M.: Predicted hygroscopic growth of sea salt aerosol. *J. Geophys. Res.-Atmos.*, 106, 28259-28274, 2001.
- Mishchenko, M. I., Geogdzhayev, I. V., Cairns, B., Rossow, W. B. and Lacis, A. A.: Aerosol retrievals over the ocean using channel 1 and 2 AVHRR data: A sensitivity analysis and preliminary results, *Appl. Opt.*, 38, 7325-7341, doi:10.1364/AO.38.007325, 1999.

- Monahan, E. C., D. E. Spiel, and K. L. Davidson: A model of marine aerosol generation via whitecaps and wave disruption, in *Oceanic Whitecaps and Their Role in Air-Sea Exchange Processes*, edited by E.C. Monahan and G. MacNiocaill, 167–174, Springer, New York, 1986.
- Morcrette, J.-J., Boucher, O., Jones, L., Salmond, D., Bechtold, P., Beljaars, A., Benedetti, A., Bonet, A., Kaiser, J. W., Razinger, M., Schulz, M., Serrar, S., Simmons, A. J., Sofiev, M., Suttie, M., Tompkins, A. M., and Untch, A.: Aerosol analysis and forecast in the European Centre for Medium-Range Weather Forecasts Integrated Forecast System: Forward modeling, *J. Geophys. Res.*, 114, D06206, doi:10.1029/2008JD011235, 2009.
- Murphy, D. M.: Little net clear-sky radiative forcing from recent regional redistribution of aerosols, *Nature Geoscience*, 6, 258-262, 2013.
- Obukhov, A.M : Turbulence in an atmosphere with a non-uniform temperature (English Translation). *Boundary-Layer Meteorology* 2: 7–29, 1971.
- Olivier J., J. Peters, C. Granier, G. Petron, J.F. Muller and S. Wallens, Present and future surface emissions of atmospheric compounds , POET report #2, EU project EVK2-1999-00011, 2003.
- O'Neill, N.T., T.F.Eck, B.N.Holben, A.Smirnov, O.Dubovik, and A.Royer: Bimodal size distribution influences on the variation of Angstrom derivatives in spectral and optical depth space, *J. Geophys. Res.*, 106, 9787-9806, 2001.
- O'Neill, N. T., Eck, T. F., Smirnov, A., Holben, B. N., and Thulasiraman S.: Spectral discrimination of coarse and fine mode optical depth. *J. Geophys. Res.*, 108, D05212, doi:10.1029/2002JD002975, 2003.
- Pankow, J. F., An absorption model of gas/particle partitioning of organic compounds in the atmosphere, *Atmos. Environ.*, 28, 189-193, 1994.
- Pérez, C., Haustein, K., Janjic, Z., Jorba, O., Huneeus, N., Baldasano, J. M., Black, T., Basart, S., Nickovic, S., Miller, R. L., Perlwitz, J. P., Schulz, M., and Thomson, M.: Atmospheric dust modeling from meso to global scales with the online NMMB/BSC-Dust model – Part 1: Model description, annual simulations and evaluation, *Atmos. Chem. Phys.*, 11, 13001–13027, doi:10.5194/acp-11-13001-2011, 2011.
- Reid, J. S., R. Koppmann, T. Eck, and D. Eleuterio: A review of biomass burning emissions part II: Intensive physical properties of biomass burning particles, *Atmos. Chem. Phys.*, 5, 99–825, 2005a.
- Reid, J. S., T. Eck, S. Christopher, O. Dubovik, R. Koppmann, D. Eleuterio, B. Holben, E. Reid, and J. Zhang: A review of biomass burning emissions part III: Intensive optical properties of biomass burning particles, *Atmos. Chem. Phys.*, 5, 827–849, 2005b.
- Reid, J. S., Hyer, E. J., Prins, E. M., Westphal, D. L., Zhang, J., Wang, J., Christopher, S. A., Curtis, C. A., Schmidt, C. C., Eleuterio, D. P., Richardson, K. A., and Hoffman, J. P.: Global Monitoring and Forecasting of Biomass-Burning Smoke: Description of and Lessons from the Fire Locating and Modeling of Burning Emissions (FLAMBE) Program, *IEEE J. Sel. Top. Appl.*, 2, 144–162, JSTARS-2009-00034, 2009.
- Reid, J. S., N. D. Lagrosas, H. H. Jonsson, E. A. Reid, W. R. Sessions, J. B. Simpas, S. N. Uy, T. J. Boyd, S. A. Atwood, D. R. Blake, J. R. Campbell, S. S. Cliff, B. N. Holben, R. E. Holz, E. J. Hyer, P. Lynch, S. Meinardi, D. J. Posselt, K. A. Richardson, S. V. Salinas, A. Smirnov, Q. Wang, L. E. Yu, and J. Zhang, Observations of the temporal variability in aerosol properties and their relationships to meteorology in the summer monsoonal South China Sea/East Sea: the role of monsoonal flows, the Madden–Julian Oscillation, tropical cyclones, squall lines and cold pools. *Atmos. Chem. Phys. Discuss.*, 14, 20521-20584, 2014.
- Reid, J. S., et al.: Observing and Understanding the Southeast Asian Aerosol System by Remote Sensing: An Initial Review and Analysis for the Seven Southeast Asian Studies (7SEAS) Program. *Atmos. Res.* 122, 403-468, 2013.
- Reid., J. S., Xian, P., Hyer, E. J., Flatau, M. K., Ramirez, E. M., Turk, F. J., Sampson, C. R., Zhang, C.,

- Fukada, E. M., and Maloney, E. D., Multi-scale meteorological conceptual analysis of observed active fire hotspot activity and smoke optical depth in the Maritime Continent, *Atmos. Chem. Phys.*, 12, 1–31, 2012.
- Remer, L. A., Kleidman, R. G., Levy, R. C., Kaufman, Y. J., Tanré, D., Mattoo, S., Martins, J. V., Ichoku, C., Koren, I., Yu, H. and Holben, B. N.: Global aerosol climatology from the MODIS satellite sensors, *J. Geophys. Res.-Atmos.*, 113, D14S07, doi:10.1029/2007JD009661, 2008.
- Remer, L. A., Y. J. Kaurman, D. Tanre, S. Mattoo, D. A. Chu, J. V. Martins, R.-R. Li, C. Ichoku, R. C. Levy, R. G. Kleidman, T. F. Eck, E. Vermote, and B. N. Holben: The MODIS aerosol algorithm, products, and validation, *J. Atmos. Sci.*, 62, 947–973, 2005.
- Reynolds, R. W., Folland, C. K., and Parker, D. E.: Biases in satellite-derived sea-surface-temperature data, *Nature*, 341, 728-731, 1989.
- Ridley, D. A., C. L. Heald, and J. M. Prospero: What Controls the Recent Changes in African Mineral Dust Aerosol Across the Atlantic? *Atmos. Chem. Phys.* 14, 5735–5747, 2014.
- Ritchie, H.: Semi-Lagrangian Advection on a Gaussian Grid, *Mon. Wea. Rev.*, 115, 608-619, 1987.
- Robock, A.: Satellite data contamination, *Nature*, 341, 695-695, 1989.
- Saltzman, E.S., D.B. King, K. Holmen, C. Leck : Experimental determination of the diffusion coefficient of dimethylsulfide in water. *J. Geophys. Res.*, 98, 16481–16486, 1993.
- Sapiano, M. R. P. and P. A. Arkin: An intercomparison and validation of high resolution satellite precipitation estimates with three-hourly gauge data. *J. Hydromet.*, 10, 149-166, 2009.
- Sekiyama, T. T., T. Y. Tanaka, A. Shimizu, and T. Miyoshi: Data assimilation of CALIPSO aerosol observations, *Atmos. Chem. Phys.*, 10, 39–49, 2010.
- Sen, P. K.: "Estimates of the regression coefficient based on Kendall's tau", *J. Amer. Stat. Association*, 63, 1379–1389, 1968.
- Sessions, W. R., Reid, J. S., Benedetti, A., Colarco, P. R., da Silva, A., Lu, S., Sekiyama, T., Tanaka, T. Y., Baldasano, J. M., Basart, S., Brooks, M. E., Eck, T. F., Iredell, M., Hansen, J. A., Jorba, O. C., Juang, H.-M. H., Lynch, P., Morcrette, J.-J., Moorthi, S., Mulcahy, J., Pradhan, Y., Razinger, M., Sampson, C. B., Wang, J., and Westphal, D. L.: Development towards a global operational aerosol consensus: basic climatological characteristics of the International Cooperative for Aerosol Prediction Multi-Model Ensemble (ICAP-MME), *Atmos. Chem. Phys.*, 15, 335-362, 2015.
- Shi, Y., J. Zhang, J. S. Reid, B. Liu, and R. Deshmukh: Multi-sensor analysis on data-assimilation-quality MISR aerosol products, Abstract A53C-0358 presented at 2011 Fall Meeting, AGU, San Francisco, Calif., 5-9 Dec, 2011c.
- Shi, Y., Zhang, J., Reid, J. S., Holben, B., Hyer, E. J., and Curtis, C.: An analysis of the collection 5 MODIS over-ocean aerosol optical depth product for its implication in aerosol assimilation, *Atmos. Chem. Phys.*, 11, 557–565, 2011a.
- Shi, Y., Zhang, J., Reid, J. S., Hyer, E. J., Eck, T. F., Holben, B. N., and Kahn, R. A.: A critical examination of spatial biases between MODIS and MISR aerosol products – application for potential AERONET deployment, *Atmos. Meas. Tech.*, 4, 2823–2836, 2011b.
- Shi, Y., Zhang, J., Reid, J. S., Liu, B., and Hyer, E. J.: Critical evaluation of cloud contamination in the MISR aerosol products using MODIS cloud mask products, *Atmos. Meas. Tech.*, 7, 1791-1801, 2014.
- Shi, Y., Zhang, J., Reid, J. S., Hyer, E. J., and Hsu, N. C.: Critical evaluation of the MODIS Deep Blue aerosol optical depth product for data assimilation over North Africa, *Atmos. Meas. Tech.*, 6, 949-969, 2013.
- Slinn, A. A., and W. G. Slinn: Predictions for particle deposition on natural waters, *Atmos. Environ.*, 14, 1013– 1016, 1980.
- Smirnov, A., B. N. Holben, T. F. Eck, O. Dubovik, and I. Slutsker: Cloud screening and quality control algorithms for the AERONET data base, *Remote Sens. Environ.*, 73, 337– 349, 2000.
- Song C., Woodcock, C. E., Seto, K. C., Lenny, M. P., Macomber, S. A., Classification and change detection

- using Landsat TM data: When and how to correct atmospheric effects? *Remote Sens. of Environ.*, 75, 230-244, 2001.
- Staniforth, A. and Côté, J.: Semi-Lagrangian integration schemes for atmospheric models—a review. *Mon. Weather Rev.*, 119, 2206–2223, 1991.
- Sun, Y., S. Solomon, A. Dai and R. W. Portmann: How often does it rain? *J. Clim.*, 19, 916-934, 2007.
- Tanaka, T. Y., Orito, K., Sekiyama, T. T., Shibata, K., Chiba, M., and Tanaka, H.: MASINGAR, a global tropospheric aerosol chemical transport model coupled with MRI/JMA98 GCM: Model description, *Pap. Meteorol. Geophys.*, 53, 119–138, 2003.
- Theil, H.: "A rank-invariant method of linear and polynomial regression analysis. I, II, III", *Nederl. Akad. Wetensch., Proc.* 53: 386–392, 521–525, 1397–1412. 1950.
- Torres, O., Bhartia, P. K., Herman, J. R., Sinyuk, A., Ginoux, P. and Holben, B.: A long-term record of aerosol optical depth from TOMS observations and comparison to AERONET measurements, *J. Atmos. Sci.*, 59, 398–413, 2002.
- Tosca, M.G., Randerson, J.T., Zender, C.S., Nelson, D.L., Diner, D.J., Logan, J.A.: Dynamics of fire plumes and smoke clouds associated with peat and deforestation fires in Indonesia. *J. Geophys. Res.* 116, 2011.
- Toth, T.D., J. Zhang, J.R. Campbell, J.S. Reid, Y. Shi, R.S. Johnson, A. Smirnov, M.A. Vaughan, and D.M. Winker: Investigating enhanced Aqua MODIS aerosol optical depth retrievals over the mid-to-high latitude Southern Oceans through intercomparison with co-located CALIOP, MAN, and AERONET data sets, *J. Geophys. Res.-Atmos.*, 118, 4700-4714, 2013.
- Uppala, S.M., Kållberg, P.W., Simmons, A.J., Andrae, U., da Costa Bechtold, V., Fiorino, M., Gibson, J.K., Haseler, J., Hernandez, A., Kelly, G.A., Li, X., Onogi, K., Saarinen, S., Sokka, N., Allan, R.P., Andersson, E., Arpe, K., Balmaseda, M.A., Beljaars, A.C.M., van de Berg, L., Bidlot, J., Bormann, N., Caires, S., Chevallier, F., Dethof, A., Dragosavac, M., Fisher, M., Fuentes, M., Hagemann, S., Hólm, E., Hoskins, B.J., Isaksen, I., Janssen, P.A.E.M., Jenne, R., McNally, A.P., Mahfouf, J.-F., Morcrette, J.-J., Rayner, N.A., Saunders, R.W., Simon, P., Sterl, A., Trenberth, K.E., Untch, A., Vasiljevic, D., Viterbo, P., and Woollen, J.: The ERA-40 re-analysis. *Quart. J. R. Meteorol. Soc.*, 131, 2961-3012, 2005.
- van der Werf, G.R., et al.: Continental-scale partitioning of fire emissions during the 1997 to 2001 El Nino/La Nina period. *Science* 303, 73–76. 2004.
- Walcek, C. J., R. A. Brost, J. S. Chang and M. L. Wesely: SO<sub>2</sub>, sulfate and HNO<sub>3</sub> deposition velocities computed using regional landuse and meteorological data. *Atmos. Environ.*, 20, 949-964, 1986.
- Walker, A. L., M. Liu, S. D. Miller, K. A. Richardson, and D. L. Westphal: Development of a dust source database for mesoscale forecasting in southwest Asia, *J. Geophys. Res.*, 114, D18207, doi:10.1029/2008JD011541, 2009.
- Wang, Chunzai, Shenfu Dong, Amato T. Evan, Gregory R. Foltz, Sang-Ki Lee: Multidecadal covariability of north atlantic sea surface temperature, african dust, sahel rainfall, and atlantic hurricanes. *J. Climate*, 25, 5404–5415. 2012.
- Wang, J., Ge, C., Yang, Z., Hyer, E. J., Reid, J. S., Chew, B. N., Mahmud, M., Zhang, Y., Zhang, M., Mesoscale modeling of smoke transport over the Southeast Asian Maritime Continent: Interplay of sea breeze, trade wind, typhoon, and topography, *Atmos. Res.*, 122, 486-503, 2013.
- Weatherhead, E. C., Reinsel, G. C., Tiao, G. C., Meng, X.-L., Choi, D., Cheang, W.-K., Keller, T., DeLuisi, J., Wuebbles, D. J., Kerr, J. B., Miller, A. J., Oltmans, S. J., and Frederick, J. E.: Factors affecting the detection of trends: Statistical considerations and applications to environmental data, *J. Geophys. Res.*, 103(D14), 17149–17161, 1998.
- Weaver, C., da Silva, A., Chin, M., Ginoux, P., Dubovik, O., Flittner, D., Zia, A., Remer, L., Holben, B., and Gregg, W.: Direct insertion of MODIS radiances in a global aerosol transport model, *J. Atmos. Sci.*, 64, 808–827, 2007.
- Westphal, D. L., Curtis, C. A., Liu, M., and Walker, A. L.: Operational aerosol and dust storm forecasting,

- in WMO/GEO Expert Meeting on an International Sand and Dust Storm Warning System, IOP Conference Series Earth and Environmental Science, 7, doi: 10.1088/1755-1307/7/1/012007, 2009.
- Westphal, D. L., O. B. Toon, and T. N. Carlson: A case study of mobilization and transport of Saharan dust. *J. Atmos. Sci.*, 45, 2145-2175, 1988.
- Wiedinmyer, C., S.K. Akagi, R.J. Yokelson, L.K. Emmons, J.A. Al-Saadi, J.J. Orlando, and A.J. Soja: The Fire INventory from NCAR (FINN): A high resolution global model to estimate the emissions from open burning. *Geoscientific Model Development*, 4, 625-641, 2011.
- Wilcox E. M. and V. Ramanathan: The impact of observed precipitation upon the transport of aerosols from South Asia, *Tellus-B*, 56, 435-450, 2004.
- Wilkinson, S. M., Dunn, S., Ma, S.: The vulnerability of the European air traffic network to spatial hazards, *Natural hazards*, 60, 1027-1036, 2012
- Witek, M. L., P. J. Flatau, P. K. Quinn, and D. L. Westphal: Global sea-salt modeling: Results and validation against multicampaign shipboard measurements, *J. Geophys. Res.*, 112, 2007.
- Xian, P., J. S. Reid, J. F. Turk, E. J. Hyer and D. L. Westphal: Impact of models versus satellite measured tropical precipitation on regional smoke optical thickness in an aerosol transport model, *Geophys. Res. Lett.*, 36, L16805, doi:10.1029/2009GL038823, 2009.
- Xian, P., J. S. Reid, S. A. Atwood, R. S. Johnson, E. J. Hyer, D. L. Westphal, W. Sessions: Smoke aerosol transport patterns over the Maritime Continent. *Atmos. Res.*, 122, 469-485, 2013.
- Young, I. R., S. Zieger, and A. V. Babanin: Global trends in wind speed and wave height, *Science*, 332, 451-455, 2011.
- Zhang, J. and Reid, J. S.: A decadal regional and global trend analysis of the aerosol optical depth using a data-assimilation grade over-water MODIS and Level 2 MISR aerosol products, *Atmos. Chem. Phys.*, 10, 10949-10963, 2010.
- Zhang, J. and Reid, J. S.: An analysis of clear sky and contextual biases using an operational over ocean MODIS aerosol product, *Geophys. Res. Lett.*, 36, L15824, doi:10.1029/2009GL038723, 2009.
- Zhang, J. and Reid, J. S.: MODIS Aerosol Product Analysis for Data Assimilation: Assessment of Level 2 Aerosol Optical Thickness Retrievals, *J. Geophys. Res.-Atmos.*, 111, 22207, doi:10.1029/2005JD006898, 2006.
- Zhang, J., J. R. Campbell, E. J. Hyer, J. S. Reid, D. L. Westphal, and R. S. Johnson: Evaluating the impact of multisensory data assimilation on a global aerosol particle transport model, *J. Geophys. Res. Atmos.*, 119, 4674-4689, 2014.
- Zhang, J., J. R. Campbell, J. S. Reid, D. L. Westphal, N. L. Baker, W. F. Campbell, and E. J. Hyer: Evaluating the impact of assimilating CALIOP-derived aerosol extinction profiles on a global mass transport model, *Geophys. Res. Lett.*, 38, L14801, doi:10.1029/2011GL047737, 2011.
- Zhang, J., Reid, J. S., Westphal, D. L., Baker, N. L., and Hyer, E. J.: A system for operational aerosol optical depth data assimilation over global oceans, *J. Geophys. Res.*, 113, D10208, doi:10.1029/2007JD009065, 2008.
- Zhang, Q., et al: Ubiquity and dominance of oxygenated species in organic aerosols in anthropogenically-influenced Northern Hemisphere midlatitudes, *Geophys. Res. Lett.*, 34, L13801, doi:10.1029/2007GL029979. 2007.

1161

1162

1163 | Table 1. Optical properties for dry aerosol particles at ~~550nm~~550 nm in NAAPS.

Species	$a_{eff}(\mu\text{m})$	$\alpha_{ext}(\text{m}^2 \text{g}^{-1})$	$\alpha_{scat}(\text{m}^2 \text{g}^{-1})$	$\alpha_{abs}(\text{m}^2 \text{g}^{-1})$	$\omega_0$	$g$
ABF	0.14	3.48	3.13	0.35	0.90	0.60
Dust	2.50	0.59	0.52	0.07	0.88	0.73
Smoke	0.17	4.48	3.99	0.50	0.89	0.58
Sea Salt	1.50	1.42	1.41	0.01	0.99	0.68

1164 where  $\alpha_{ext}$ ,  $\alpha_{scat}$ , and  $\alpha_{abs}$  are the bulk mass extinction, scattering, and absorption efficiencies,  $\omega_0$  the  
1165 single scattering albedo and  $g$  the asymmetry factor.  $a_{eff}$  is the bulk effective radius. "ABF" stands for  
1166 anthropogenic and biogenic fine particles.

1167

1168 Table 2. List of AERONET sites for further validation and statistics of the reanalysis total AOT at  
1169 | ~~550nm~~550 nm compared with AERONET at these sites for December 2011-November 2012 breaking into  
1170 two seasons DJFMAM (winter) and JJASON (summer). The selected sites and time periods match  
1171 Sessions et al. (2015), where the International Cooperative for Aerosol Prediction (ICAP) Multi Model  
1172 Ensemble (ICAP-MME) AOT is described and evaluated. The mean of total AOT of AERONET L2 data, the  
1173 paired reanalysis data bias, root mean square error (RMSE), square of the Pearson correlation  
1174 | coefficient ( $r^2$ ) and the total number of AERONET ~~6-hly~~6-hourly data (N) are shown. Values in bold, bold  
1175 with underline and italic mean that the reanalysis is equally good, better and worse than the ICAP MME  
1176 mean respectively (Such comparison is not available in terms of  $r^2$  or for the fine mode AOT).

1177 Note: Correlation is not calculated for sites with dynamical range of the AOT data less than 0.1;  
1178 correlation is marked with "N/A\*" for these sites. "N/A" means data is not available.

1179 Seasonal AOT means for sites with only a few AERONET data (N) may not be representative.



Site	Location	Main Aerosol type	Mean AERONET total <del>550nm</del> 550 nm AOT		Bias		RMSE		r <sup>2</sup>		N	
			winter	summer	winter	summer	winter	summer	winter	summer	winter	summer
Alta Floresta	Brazil, 9S, 56W	Smoke	0.12	0.29	<b>0.00</b>	-0.03	<b>0.05</b>	<b>0.11</b>	0.49	0.82	35	203
Baengnyeong	Yellow Sea, 37N, 124E	ABF, Dust	0.39	0.34	<b>0.04</b>	<b>0.00</b>	<b>0.16</b>	<b>0.18</b>	0.77	0.75	213	215
Banizoumbou	Sahel, 13N, 2E	Dust	0.67	0.42	-0.11	<b>-0.08</b>	0.35	<b>0.21</b>	0.53	0.51	493	396
Beijing	China, 39N, 116E	ABF, Dust	0.60	0.62	-0.14	-0.17	0.50	<b>0.45</b>	0.54	0.76	322	110
Capo Verde	Sub-tro. Atlantic, 16N, 22W	Dust	0.36	0.39	<b>0.02</b>	<b>0.00</b>	<b>0.12</b>	0.12	0.88	0.77	283	312
Cart Site	Great Plains, 36N, 97W	Clean	0.10	0.14	<b>0.00</b>	<b>-0.01</b>	0.05	<b>0.05</b>	0.65	0.63	335	419
Chapais	Quebec, 49N, 74W	Clean	N/A	0.12	N/A	<b>0.00</b>	N/A	<b>0.05</b>	N/A	0.72	0	112
Chiang Mai	Thailand, 18N, 98E	Smoke	0.63	0.23	<b>-0.14</b>	-0.05	<b>0.27</b>	0.11	0.82	0.44	297	161
Crozet Island	Southern Ocean, 46S, 51E	Sea Salt	0.04	0.05	0.03	<b>0.03</b>	<b>0.05</b>	<b>0.05</b>	N/A*	N/A*	18	41
Gandhi College	Rural India, 25N, 84E	Dust, ABF	0.60	0.70	<b>-0.08</b>	<b>-0.08</b>	<b>0.15</b>	<b>0.30</b>	0.71	0.35	315	311
GSFC	EAST CONUS, 38N, 76W	ABF	0.11	0.18	<b>0.00</b>	<b>-0.01</b>	<b>0.05</b>	<b>0.07</b>	0.63	0.71	272	297
Ilorin	Sahel, 8N, 4E	Smoke, Dust	0.99	0.30	<b>-0.09</b>	<b>0.02</b>	<b>0.31</b>	0.13	0.75	0.55	411	182
Kanpur	Urban India, 26N, 80E	ABF, Dust	0.61	0.70	<b>-0.08</b>	<b>-0.02</b>	<b>0.19</b>	<b>0.27</b>	0.61	0.21	385	281
Minsk	Western Asia, 53N, 27E	ABF, Smoke	0.14	0.15	<b>0.00</b>	<b>-0.01</b>	0.06	<b>0.07</b>	0.52	0.51	156	180
Moldova	Eastern Europe, 47N, 28E	ABF	0.19	0.17	<b>0.00</b>	<b>0.00</b>	<b>0.07</b>	<b>0.07</b>	0.42	0.59	197	347
Monterey	WEST CONUS, 36N, 121W	Clean	0.08	0.07	<b>0.02</b>	<b>-0.01</b>	<b>0.04</b>	<b>0.03</b>	0.53	0.31	80	77
Palma de Mallorca	Mediterranean, 39N, 2E	Dust, ABF	0.08	0.20	<b>0.00</b>	-0.02	<b>0.02</b>	<b>0.06</b>	0.85	0.85	24	401
Ragged Point	Caribbean, 13N, 59W	African Dust	0.15	0.21	<b>0.00</b>	<b>0.01</b>	<b>0.05</b>	0.06	0.81	0.87	285	227
Rio Branco	Brazil, 9S, 67W	Smoke	0.08	0.22	<b>0.00</b>	<b>-0.02</b>	0.04	<b>0.08</b>	N/A*	0.86	144	328
Singapore	Maritime Cont., 1N, 103E	ABF, Smoke	0.31	0.47	-0.12	-0.16	0.20	0.24	0.15	0.55	71	192
Solar Village	Southwest Asia, 24N, 46E	Dust	0.63	0.38	<b>0.02</b>	0.07	0.27	0.13	0.25	0.68	77	318

1180

1181

1182

1183 Table 3. Same as Table 2, except for fine-mode AOT at ~~550nm~~550 nm.

Site	Mean AERONET fine AOT		Bias		RMSE		r <sup>2</sup>		N	
	winter	summer	winter	summer	winter	summer	winter	summer	winter	summer
Alta Floresta	0.07	0.21	0.02	0.02	0.04	0.11	0.49	0.77	35	203
Baengnyeong	0.26	0.25	0.04	0.01	0.14	0.16	0.75	0.74	213	215
Banizoumbou	0.15	0.07	-0.03	0.07	0.14	0.11	0.17	0.16	493	396
Beijing	0.37	0.47	-0.05	-0.10	0.32	0.34	0.57	0.79	322	110
Capo Verde	0.08	0.06	0.01	0.03	0.07	0.05	0.33	0.30	283	312
Cart Site	0.06	0.09	0.01	0.02	0.03	0.04	0.69	0.70	335	419
Chapais	N/A	0.08	N/A	0.02	N/A	0.05	0.00	0.73	0	112
Chiang Mai	0.50	0.14	-0.04	0.02	0.22	0.08	0.82	0.48	297	161
Crozet Island	0.01	0.02	-0.01	-0.01	0.01	0.01	N/A*	N/A*	18	41
Gandhi College	0.31	0.43	0.02	0.05	0.11	0.23	0.71	0.41	315	311
GSFC	0.07	0.13	0.01	0.01	0.04	0.06	0.59	0.72	272	297
Ilorin	0.36	0.13	0.00	0.08	0.15	0.13	0.50	0.23	411	182
Kanpur	0.34	0.41	0.01	0.06	0.14	0.26	0.71	0.27	385	281
Minsk	0.09	0.10	0.01	0.01	0.04	0.05	0.53	0.47	156	180
Moldova	0.11	0.11	0.02	0.02	0.06	0.06	0.44	0.59	197	347
Monterey	0.03	0.04	0.02	0.00	0.02	0.02	N/A*	N/A*	80	77
Palma de Mallorca	0.05	0.09	0.00	0.00	0.02	0.03	0.91	0.61	24	401
Ragged Point	0.03	0.03	0.02	0.01	0.03	0.02	N/A*	N/A*	285	227
Rio Branco	0.04	0.16	0.01	0.03	0.02	0.08	N/A*	0.86	144	328
Singapore	0.21	0.34	-0.04	-0.07	0.14	0.18	0.13	0.58	71	192
Solar Village	0.11	0.13	0.07	0.06	0.09	0.07	0.09	0.36	77	318

1184

1185

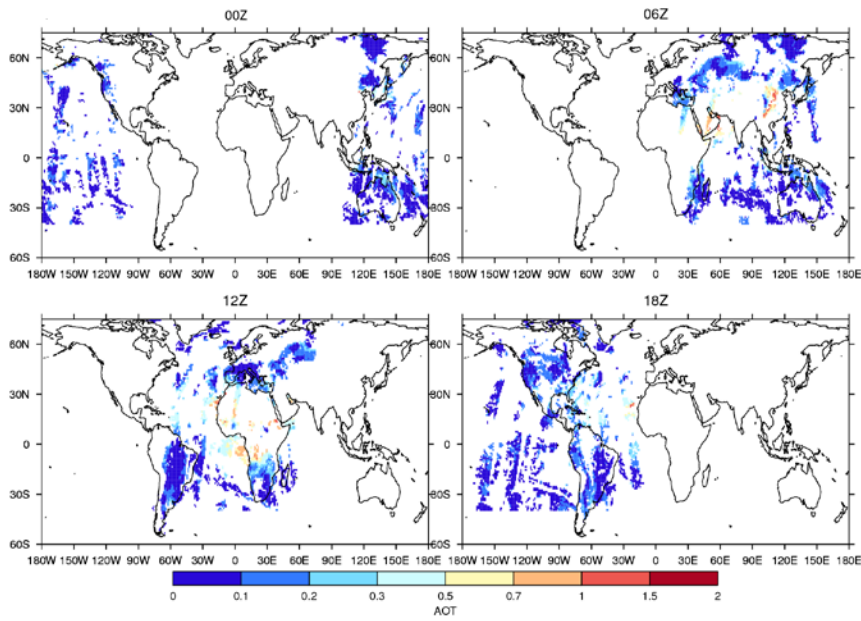
1186

1187 | Table 4, same as Table 2, except for coarse-mode AOT at ~~550nm~~550 nm and for sites in which the coarse  
1188 mode is dominated by dust.

1189

Site	Mean AERONET coarse AOT		Bias		RMSE		r <sup>2</sup>		N	
	winter	summer	winter	summer	winter	summer	winter	summer	winter	summer
Baengnyeong	0.13	0.09	<b>0.00</b>	<b>-0.01</b>	0.07	<b>0.05</b>	0.47	0.63	213	215
Banizoumbou	0.52	0.35	-0.08	-0.15	0.29	0.23	0.50	0.55	493	396
Beijing	0.24	0.15	-0.09	-0.07	0.31	0.16	0.12	0.37	322	110
Capo Verde	0.28	0.33	<b>0.01</b>	-0.04	<b>0.09</b>	0.12	0.89	0.74	283	312
Gandhi College	0.29	0.27	-0.10	-0.13	0.14	0.23	0.50	0.57	315	311
Ilorin	0.63	0.17	-0.09	-0.06	0.30	0.11	0.65	0.49	411	182
Kanpur	0.27	0.29	-0.09	<b>-0.09</b>	0.14	0.15	0.65	0.69	385	281
Palma de Mallorca	0.03	0.11	<b>0.00</b>	-0.02	<b>0.01</b>	0.05	0.53	0.83	24	401
Ragged Point	0.12	0.18	<b>-0.02</b>	<b>-0.01</b>	<b>0.06</b>	<b>0.06</b>	0.72	0.85	285	227
Solar Village	0.52	0.25	-0.05	<b>0.01</b>	0.24	0.10	0.24	0.71	77	318

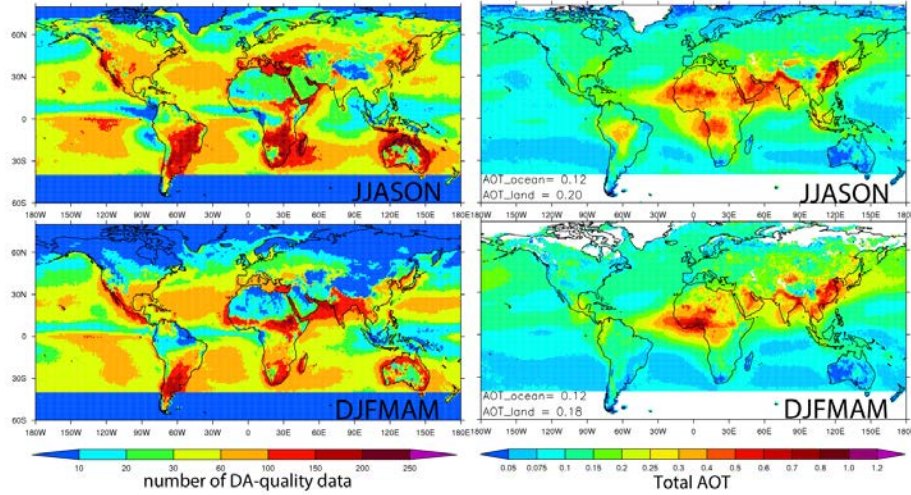
1190



1191

1192 Figure 1. An example of the general pattern of data coverage from MODIS (Aqua + Terra) and MISR for  
1193 each AOT assimilation cycle at the valid time of the analysis, ie., 0, 6, 12 and 18 UTC, in NAVDAS-AOT.  
1194 The MODIS and MISR AOT data displayed here is after strict QA/QC processes for Aug 11, 2011. The  
1195 MODIS and MISR data assimilated in each NAVDAS-AOT cycle were acquired in a 6-hour range centered  
1196 on the nominal valid time of the analysis.

1197



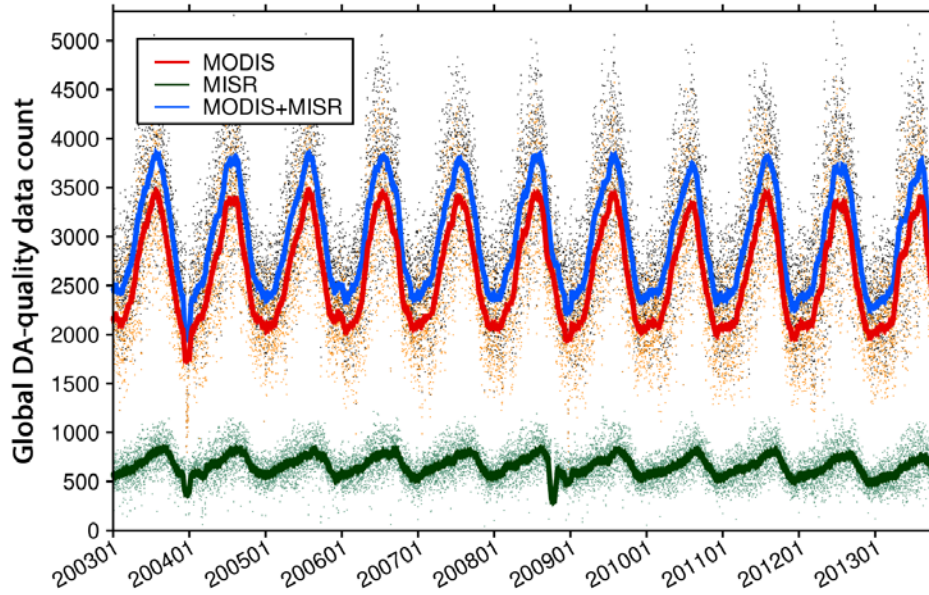
1198

1199 | Figure 2. Properties of the ~~6-hrly~~6-hourly 1x1 degree MODIS+MISR data assimilation quality AOT data  
1200 | for JJASON (June-November, upper) and DJFMAM (Previous year December-May, lower) averaged over  
1201 | 2003-2013 (June 2003-May 2013): Left) total number of the DA-quality data, Right) seasonal mean of  
1202 | the total AOT at ~~550nm~~550 nm. Blank area indicates no available data. Annotations at the bottom left in  
1203 | the AOT figures show the area mean AOTs over ocean and over land averaged for 40°S-60°N.

1204

1205

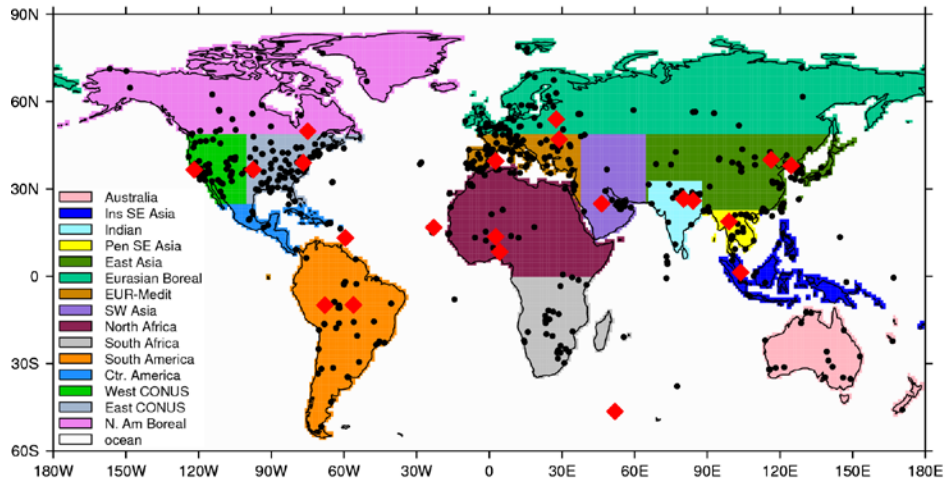
1206



1207

1208 | Figure 3. The time series of ~~6-hrly6-hourly~~ data count of the global 1x1 grid MODIS (Terra+Aqua) (red),  
1209 | MISR (green), and fused MODIS-MISR data assimilation quality AOT (blue). Dots show ~~6-hrly6-hourly~~  
1210 | data counts, and the solid lines represent the 30-day running average. The seasonal variation of the data  
1211 | volume is mainly related to the fact that more AOT data are discarded for the southern hemisphere high  
1212 | latitudes than the northern hemisphere high latitudes considering cloud contamination (see text for  
1213 | details).

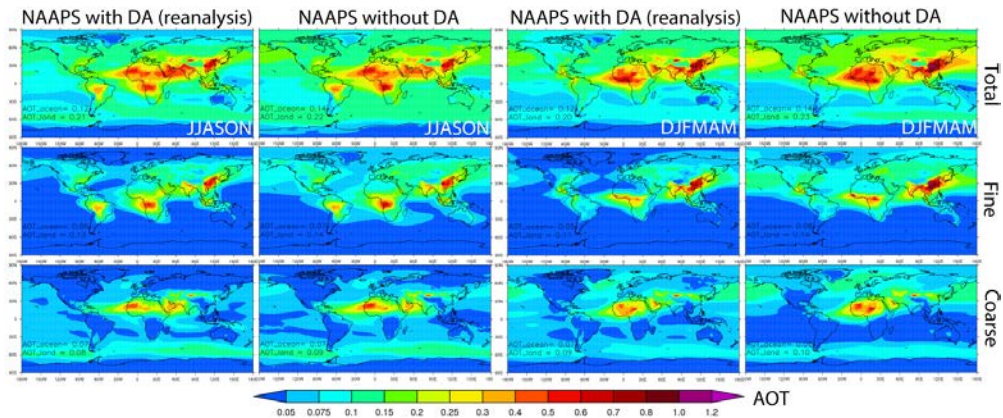
1214



1215

1216 Figure 4. Selection of regions for this study. Antarctica is excluded. All AERONET sites that have valid L2  
 1217 data for the study period (2003-2013) are in black dots. The selected sites for detailed validation  
 1218 (Section 3.2.3) are highlighted with red diamonds.

1219

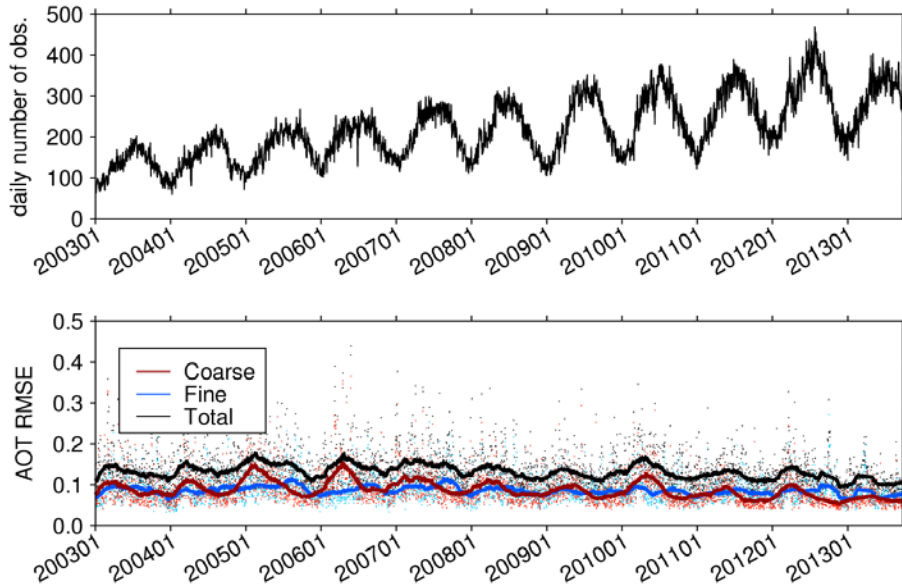


1220

1221 Figure 5. 2003-2013 averaged biseseasonal (June-November, ie., JJASON, and  
 1222 December-May, ie., DJFMAM) total (upper), fine (middle) and coarse (bottom) AOTs at ~~550nm~~550 nm  
 1223 from NAAPS with and without AOT data assimilation. Annotations at the bottom left in the figures show the area mean AOTs  
 1224 over ocean and over land averaged for 40°S-60°N.

1225



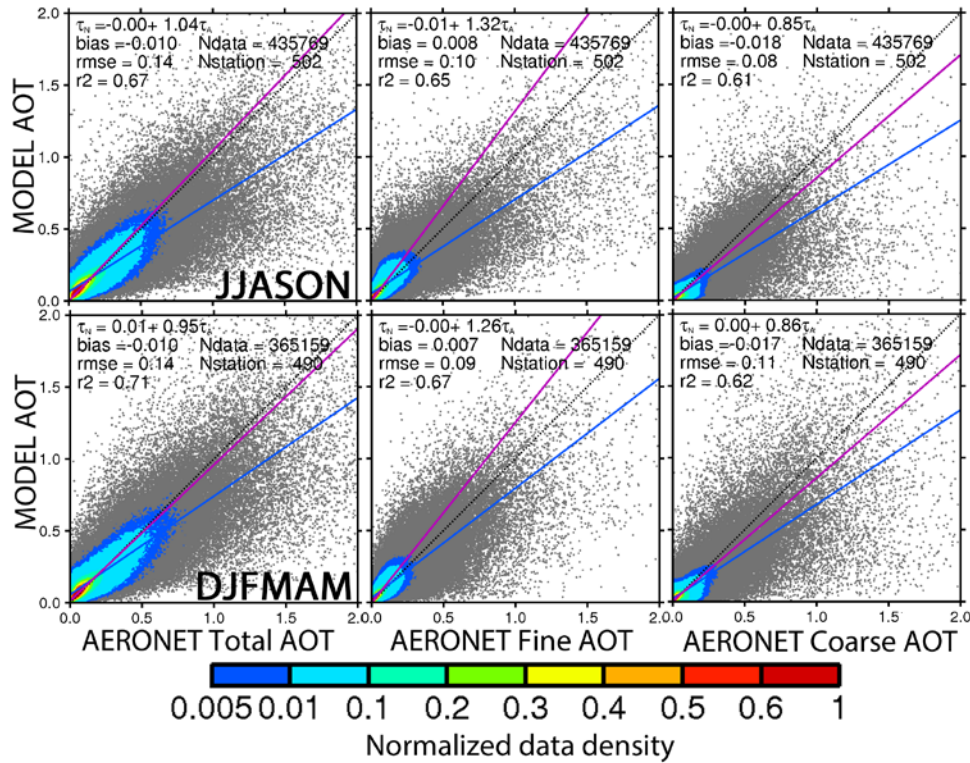


1226

1227 Figure 6. a) Time series of the daily total number of global regular AERONET L2 observations (excluding  
 1228 observations at DRAGON sites) binned into ~~6-hrly~~6-hourly intervals (to match the model output  
 1229 resolution) for the AOT reanalysis period. b) Time series of the RMSE of the reanalysis total AOT (black),  
 1230 fine-mode AOT (blue) and coarse-mode AOT (red), all at ~~550nm~~550 nm, validated with AERONET. The  
 1231 daily average 6-hr RMSEs are in small dots and the corresponding 90-day running averages are in solid  
 1232 lines.

1233

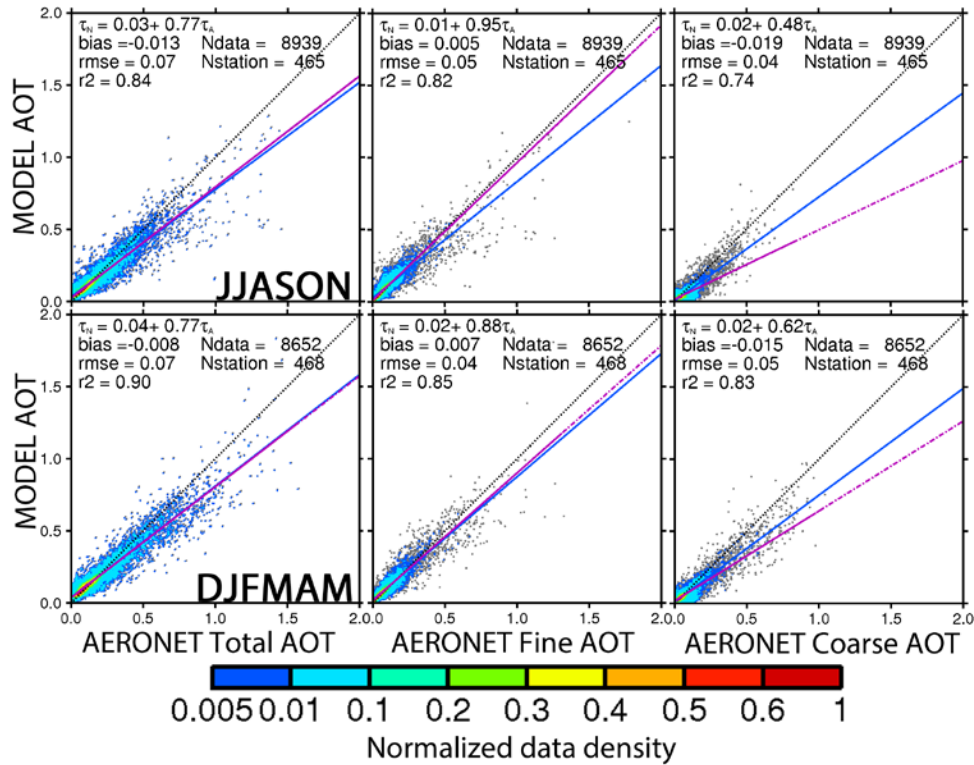
1234



1235

1236 Figure 7. Pair-wise comparison of the global 6-hourly reanalysis AOT and AERONET AOT with  
 1237 respect to total (left), fine (middle) and coarse (right) modes at 550nm for JJASON (upper) and  
 1238 DJFMAM (bottom) for the entire reanalysis time (2003-2013). The normalized data density is shown in  
 1239 color. The solid magenta line represents a Theil-Sen linear regression and the corresponding equation is  
 1240 shown, where  $\tau_N$  is the NAAPS reanalysis AOT and  $\tau_A$  is the AERONET AOT. The solid blue line is a least-  
 1241 squares linear regression and the corresponding equation is not shown. Also shown are the bias, root  
 1242 mean square error (rmse), square of the pearson's correlation coefficient ( $r^2$ ), total number of stations  
 1243 (Nstation) and total number of 6-hourly AERONET data (Ndata).

1244

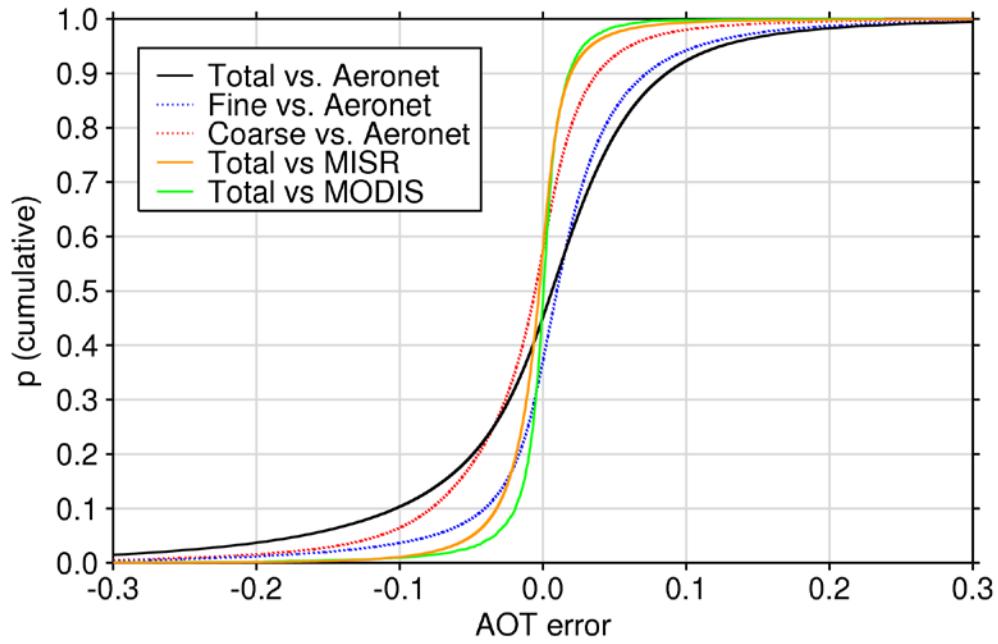


1245

1246 | Figure 8. Same as Fig. 7, except for the monthly average of pair-wised 6-hrly6-hourly mode AOTs at  
 1247 | 550nm550 nm. Monthly average is obtained only when the total number of 6-hrly6-hourly AERONET  
 1248 | data exceeds 10 to ensure temporal representativeness. The monthly average reanalysis AOT here is  
 1249 | calculated based on the available 6-hrly6-hourly data that can be paired with AERONET data.

1250

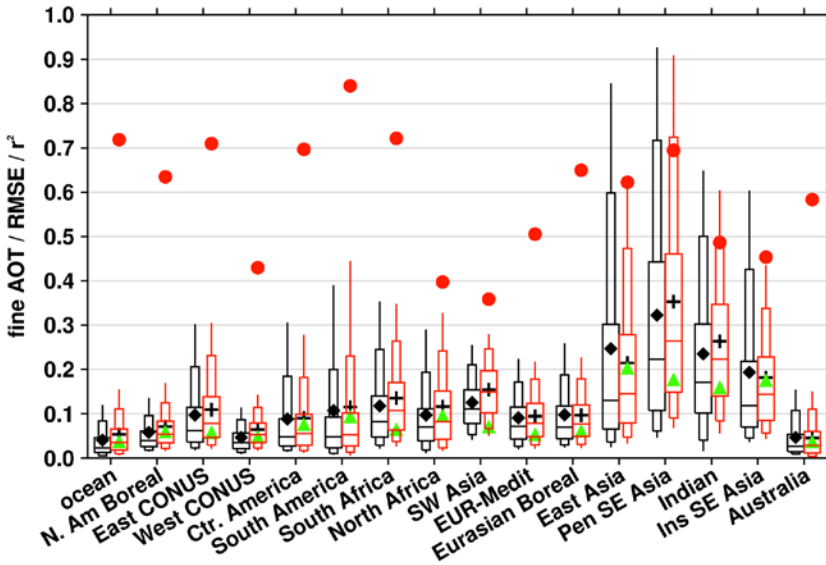
1251



1252

1253 | Figure 9. Cumulative distribution function for the reanalysis ~~6-hrly~~6-hourly AOT errors compared to  
1254 | AERONET L2, MODIS and MISR data assimilation quality data with respect to the available total, fine and  
1255 | coarse modes at ~~550nm~~550 nm for the entire reanalysis time period (2003-2013).

1256



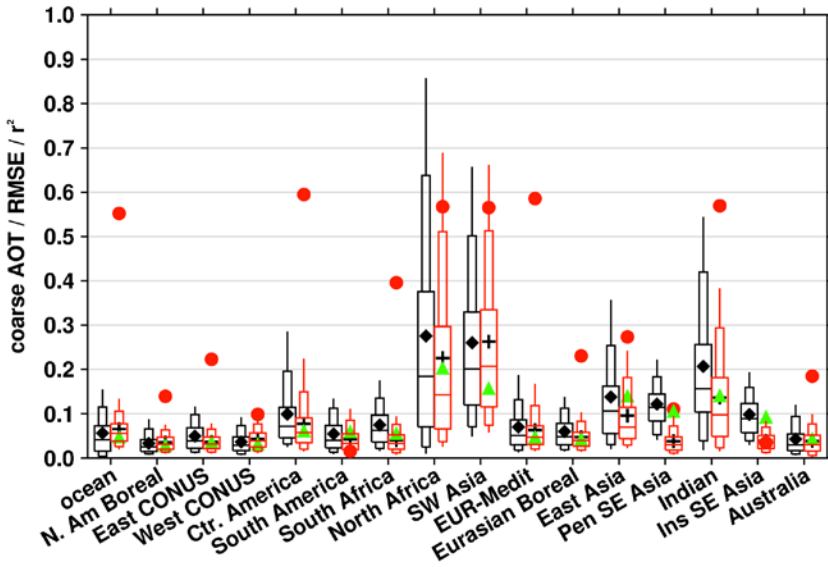
1257

1258 | Figure 10. Comparison of regional fine mode AOT at ~~550nm~~550 nm of the reanalysis (red) at 95%, 90%,  
 1259 75%, 50%, 25%, 10% and 5% percentiles to the pair-wised AERONET L2 data (black) for the regions  
 1260 defined in Figure 4 for the 10 year time period (June 2003-May 2013). Also shown are the regional mean  
 1261 of the reanalysis and AERONET fine mode AOTs in “+” and diamond respectively. Green triangles  
 1262 represent the root mean square error (RMSE) of the reanalysis. Red dots represent the square of the  
 1263 Pearson correlation coefficient ( $r^2$ ) between the reanalysis and the AERONET observations.

1264

1265

1266

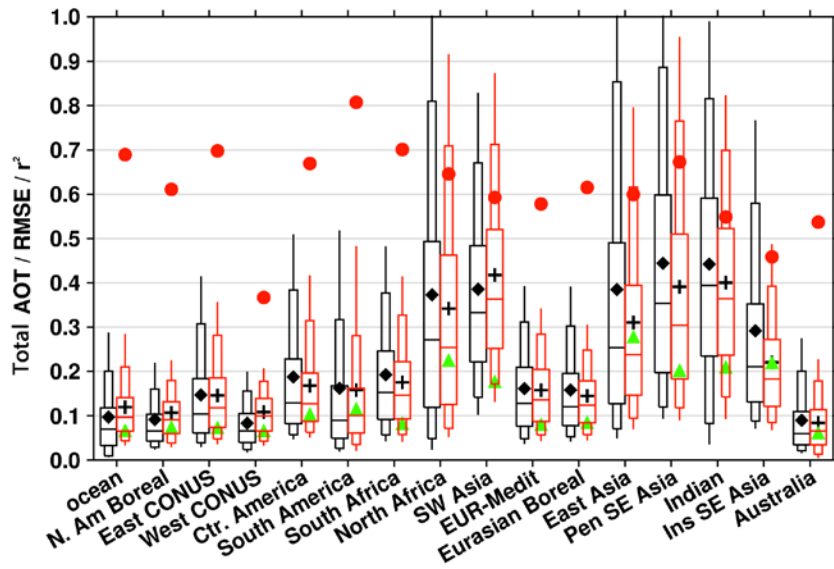


1267

1268 | Figure 11. Same as Fig. 10, except for coarse mode AOT at 550nm 550 nm.

1269

1270

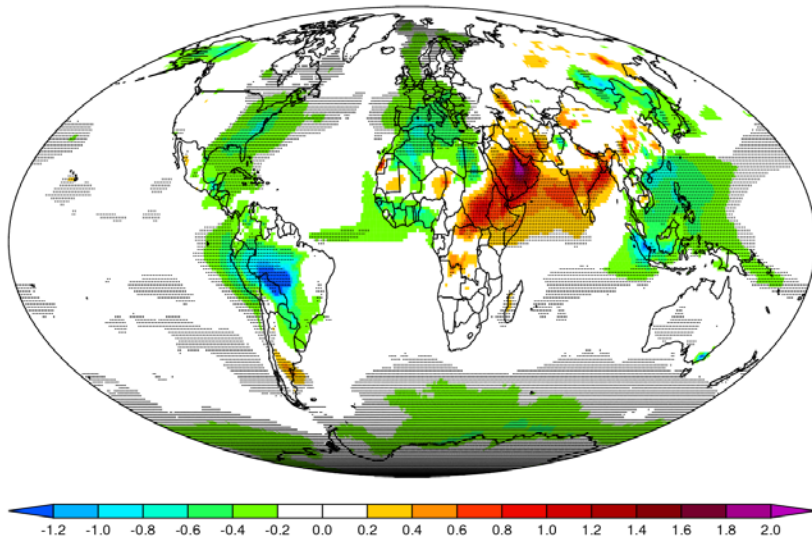


1271

1272 | Figure 12. Same as Fig. 10, except for total AOT at 550nm550 nm. Also, AOT value greater than 1.0 is  
 1273 | cropped in this figure.

1274

1275



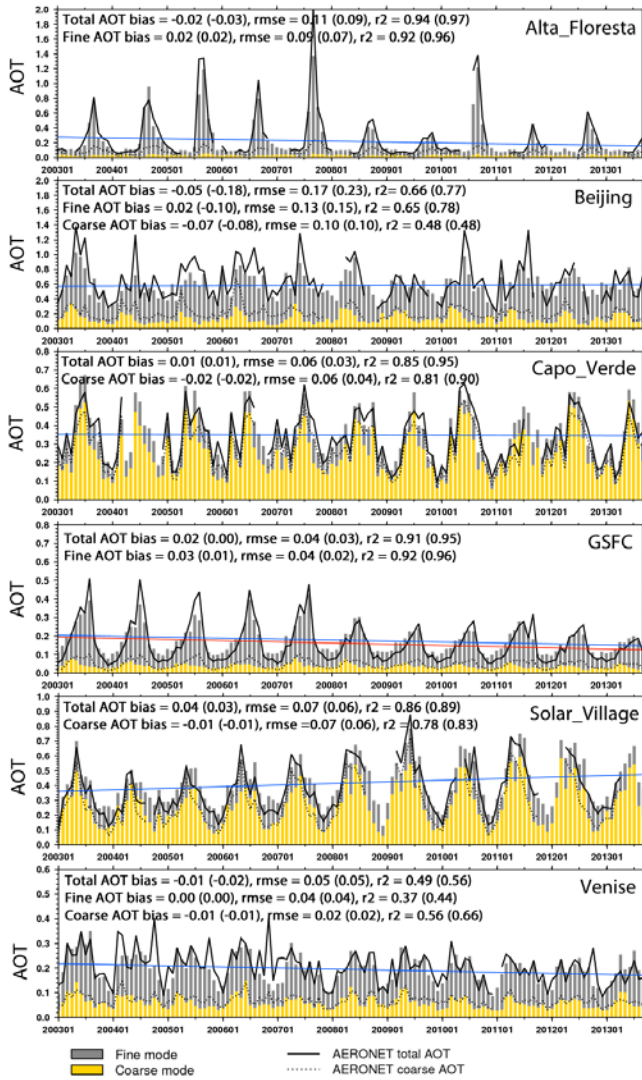
1276

1277 | Figure 13. Trends of the deseasonalized reanalysis total AOT at ~~550nm~~550 nm over 2003-2013 (unit:  
1278 100xAOT/year). The dotted areas have passed 95% statistical significance level (see text and Zhang and  
1279 Reid (2010) for details).

1280

1281





1282

1283 | Figure 14. Monthly mean ~~550nm~~550 nm reanalysis and AERONET L2 mode AOTs at 6 AERONET sites,  
 1284 Alta Floresta in the Amazon, Beijing in East Asia, Capo Verde off the west coast of North Africa, GSFC in  
 1285 East CONUS, Solar Village in Arabian Peninsula, and Venice in Italy. The solid blue line is a linear  
 1286 regression of the reanalysis total AOT. The red solid line is a linear regression of the AERONET total AOT,  
 1287 only available when there is continuous data through the time. Monthly mean AERONET AOT is obtained  
 1288 | only when the total number of ~~6-hrly~~6-hourly AERONET data exceeds 10 to ensure temporal  
 1289 representativeness. Annotations for each time series show bias, RMSE and  $r^2$  of monthly averages for  
 1290 unpaired comparisons; paired comparisons, using reanalysis values sampled to match available  
 1291 AERONET data, are shown in parentheses.

1292 APPENDIX: Impact of tuning of sources and sinks vs. AOT data assimilation upon model performance

1293 To show the relative importance of the tuning process on sources and sinks versus the AOT data  
1294 assimilation to reanalysis performance, four model runs with difference configurations were conducted.  
1295 AOT results from these four runs were inter-compared and validated with AERONET L2 data. The four  
1296 model configurations are NAAPS without tuning (that is to say the original native version of NAAPS from  
1297 which the reanalysis was originally based), NAAPS with tuning, NAAPS without tuning but with AOT data  
1298 assimilation, and the final reanalysis version, which is with both tuning and AOT assimilation. The four  
1299 model runs all cover Dec 2010-Nov 2011 one year time period. Interannual tuning was not conducted to  
1300 preserve a measure of consistency within the model itself. The AOT data assimilation process, the input  
1301 data and its pre-DA treatment are kept the same for the DA runs. The “tuning” processes on the sources  
1302 and sinks include the addition of organic aerosols, updated SO<sub>2</sub> and DMS emissions, use of CMORPH  
1303 precipitation to replace model precipitation within 30°S-30°N, usage of the FLAMBE MODIS 2-day-  
1304 maximum regionally tuned smoke emissions and applying regional tuned factors on dust erodible  
1305 fraction. For example, through the tuning exercises dust emission for 2011 is reduced from 1510 Tg to  
1306 953 Tg, and biomass turning smoke emission is reduced from 180 Tg to 85 Tg globally.

1307 The appendix table shows the ~~550nm~~550 nm total, fine and coarse mode AOT bias, RMSE, r<sup>2</sup> and  
1308 Theil-Sen linear regression slope against AERONET from the four model runs. With the tuning of sources  
1309 and sinks, RMSE decreases about half, bias and r<sup>2</sup> also significantly improved for coarse, fine and total  
1310 AOTs for the natural model run. The linear regression slope is also much closer to 1 for the fine and the  
1311 total AOTs, and about unchanged for the coarse AOT compared to the NAAPS run without sources and  
1312 sinks tuning. The absolute bias, RMSE and r<sup>2</sup> are comparable with those of the DA run without the tuning;  
1313 i.e., through the tuning process on the baseline (“NAAPS\_untuned”), similar validation result can be  
1314 obtained as through the AOT assimilation on the baseline. This indicates that the tuning process on  
1315 sources and sinks is as equally important as the AOT data assimilation process.

1316 AOT data assimilation based on the tuned NAAPS further improves the validation statistics. For  
1317 example, the RMSE is reduced about 20% for the coarse, fine and total AOTs comparing the reanalysis to  
1318 the “NAAPS\_tuned”. When comparing the DA runs (“reanalysis” vs. “DA\_untuned”), there are also  
1319 discernable improvements on bias, RMSE and  $r^2$  resulted from the tuning process. The linear regression  
1320 slope is improved for the fine AOT and about the same for the total AOT. The regression slope is  
1321 worsened for the coarse AOT (0.64 for the reanalysis), because the model, like other aerosol models,  
1322 faces challenges successfully resolving dust events over Sahel, East Asia and Indian subcontinent regions  
1323 (e.g., Sessions et. al. 2015). While the untuned model has slight high biased coarse AOT, which makes  
1324 the regression slope more tilted. The linear regression slope of the reanalysis based on all the 11-year  
1325 data is 0.85 (Fig.7) though, better than the 2011 level.

1326 The appendix Fig. 1 and Fig. 2 show the global coarse, fine and total AOT distributions from the four  
1327 model runs for the two seasons of 2011, ie., JJASON and DJFMAM respectively. For both seasons, it is  
1328 obvious that the natural NAAPS run without tunings has the most different AOT distributions and global  
1329 averages among the four runs. The three other runs look more similar to each other, which is consistent  
1330 with the validation statistics shown in appendix Table 1. For JJASON the natural NAAPS run without  
1331 tunings has the lowest global mean AOTs among the four runs, yet the highest AOTs near dust and  
1332 smoke source regions in South America and South Africa. This indicates possible excessive emissions in  
1333 these regions and excessive removals over water, which are tuned through applying smaller emission  
1334 factors for smoke and dust and lower dry deposition velocity for dust over water in the tuning process.  
1335 For both seasons, the tuned NAAPS run without DA has slight high bias in the fine AOT (see also  
1336 appendix Table 1) and the bias is slightly larger in DJFMAM than in JJASON, most probably resulted from  
1337 excessive addition of organic aerosols during boreal winter.

1338 Compared to the reanalysis, the DA run without source and sink tuning, exhibits similar global total AOT  
1339 distribution. However, some differences between the two are noticeable for the fine and coarse AOTs.  
1340 For example, over the Indian subcontinent the AOT partitioning between the fine and coarse AOTs  
1341 differs significantly. The contribution of the fine-mode aerosols to the total AOT dominates the  
1342 contribution of the coarse-mode aerosols in the reanalysis. Whereas the total AOT is predominantly  
1343 attributed to the coarse-mode aerosols in the DA run without tunings. Over the southern flank of the  
1344 Himalayas, where fine-mode aerosols from industrial and biofuel emissions often prevails over coarse-  
1345 mode (refer to Kanpur site in Tables 2-4), the fine mode fraction is increased from  $\sim 0.3$  in the DA run  
1346 without tunings to  $\sim 0.7$  in the reanalysis. This illustrates the importance of the tuning processes in  
1347 yielding a better AOT partitioning between the fine and coarse modes.

1348

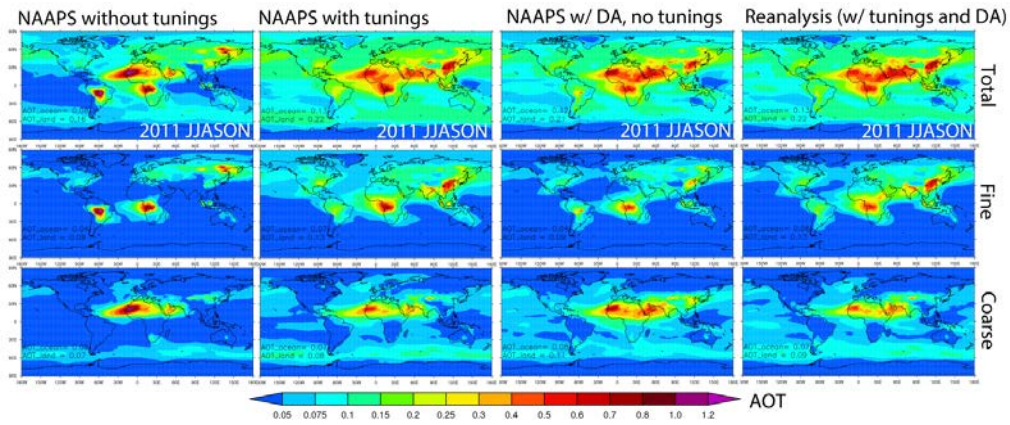
1349 | Appendix Table: Statistics of the coarse, fine and total AOTs at ~~550nm~~550 nm from four model runs  
 1350 | compared with AERONET L2 data. The four model runs are from four different model configurations,  
 1351 | including NAAPS without sources and sinks tuning, NAAPS with tuning, NAAPS without tuning but with  
 1352 | AOT data assimilation, and the reanalysis version, which is with both the tuning and the AOT  
 1353 | assimilation. The comparison is based on one year time period (Dec. 2010 to Nov. 2011). The global  
 1354 | AERONET mean is 0.085, 0.102 and 0.187 for coarse, fine and total AOT respectively, obtained with  
 1355 | averaging 97654 valid ~~6-hrly~~6-hourly L2 data from 285 stations.

	AOT Bias	RMSE	$r^2$	Regression slope
	Coarse   fine   total	Coarse   fine   total	Coarse   fine   total	Coarse   fine   total
NAAPS_untuned	0.008 -0.030 -0.022	0.17 0.19 0.26	0.33 0.05 0.15	0.59 0.69 0.81
NAAPS_tuned	-0.005 0.021 0.016	0.10 0.10 0.16	0.45 0.47 0.48	0.58 0.98 0.89
DA_untuned	0.014 -0.025 -0.011	0.09 0.11 0.14	0.58 0.41 0.56	0.90 0.75 0.80
Reanalysis	-0.013 0.006 -0.007	0.08 0.08 0.13	0.59 0.63 0.65	0.64 1.00 0.77

1356

1357

1358



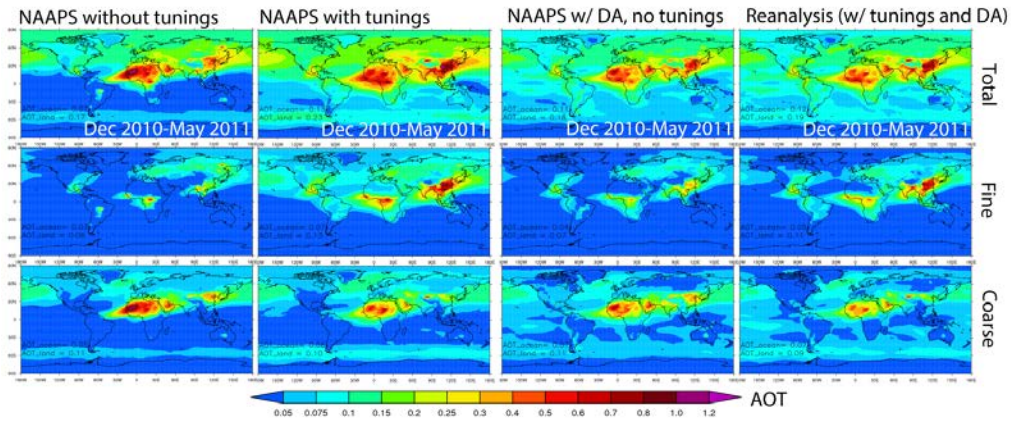
1359

1360 Appendix Figure 1. 6-month-average (Jun-Nov 2011) total (upper), fine (middle) and coarse (bottom)  
1361 | AOTs at ~~550nm~~550 nm from four NAAPS runs with different configuration: NAAPS without tuning,  
1362 NAAPS with tuning processes on sources and sinks, NAAPS without tuning but with AOT data  
1363 assimilation, and the reanalysis version, which is with both tuning and AOT assimilation. Annotations at  
1364 the bottom left in the figures show the area mean AOTs over ocean and over land averaged for 40°S-  
1365 60°N.

1366

1367

1368



1369

1370 Appendix Figure 2. Same as the Appendix Figure 1, except for Dec. 2010-May 2011 6-month-average.